








## Recent progress at the interface between nanomaterial chirality and liquid crystals\*

Diana P. N. Gonçalves <sup>a</sup>, Marianne E. Prévôt <sup>a</sup>, Şenay Üstünel <sup>a,b</sup>, Timothy Ogolla <sup>a,b</sup>, Ahlam Nemati <sup>a,b</sup>, Sasan Shadpour <sup>a,b</sup> and Torsten Hegmann <sup>a,b,c,d</sup>

<sup>a</sup>Advanced Materials and Liquid Crystal Institute, Kent State University, Kent, OH, USA; <sup>b</sup>Materials Science Graduate Program, Kent State University, Kent, OH, USA; <sup>c</sup>Department of Chemistry and Biochemistry, Kent State University, Kent, OH, USA; <sup>d</sup>Brain Health Research Institute, Kent State University, Kent, OH, USA

### ABSTRACT

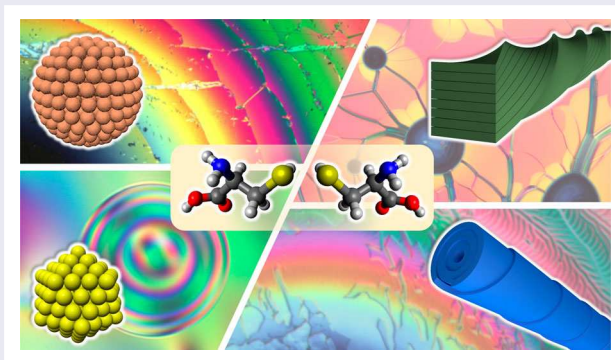
Chirality of nanomaterials is a rapidly evolving field, largely driven by the unique optical, electronic, magnetic or catalytic properties of plasmonic, magnetic and semiconductor nanomaterials among others. Liquid crystals continue to play a major role in developing a better understanding of their inherent chiroptical properties as well as serving as reporters to quantify and visualize nanomaterial chirality. Furthermore, liquid crystal phases are increasingly explored as potentially tuneable templates for the helical assembly of various types of nanomaterials. This review summarizes recent progress in this area by describing representative examples and key strategies pursued to interface nanomaterial and liquid crystal chirality. These studies focus on a range of organic and inorganic nanomaterials varying in size, shape and composition as well as on both thermotropic and lyotropic liquid crystal phases. Finally, the two materials concepts merge when liquid crystal molecules self-assemble into distinct filamentous chiral nanoshapes capable of templating other nanomaterials.

### ARTICLE HISTORY

Received 29 March 2021  
Accepted 12 May 2021

### KEYWORDS

Chirality; nanomaterials; liquid crystals; self-assembly; templating



## 1. Introduction

The research area of creating and exploring chiral nanomaterials has seen an almost exponential growth over the past two decades [1]. Not long after the trailblazing reports by Brust and Schiffrin in the mid-1990s [2, 3], making the synthesis and functionalization of metal and in particular gold nanoparticles (Au NPs) widely accessible to the global research community, reports emerged that demonstrated immense optical activities of gold

nanoclusters decorated with chiral bioorganic molecules [4, 5]. The field rapidly expanded to intrinsically chiral gold nanoclusters [6–11] and their chiral assemblies and further to increasingly sophisticated metal, semiconductor [12], carbon-based [13], ceramic [14], polymer [15, 16] as well as magnetic chiral nanostructures and assemblies [17] across many shapes and length scales [1, 18]. Mechanisms of chirality transfer and amplification have become gradually better understood, propelling research

**CONTACT** Torsten Hegmann  [thegmann@kent.edu](mailto:thegmann@kent.edu)  Advanced Materials and Liquid Crystal Institute, Kent State University, Kent, OH 44242, USA  
Materials Science Graduate Program, Kent State University, Kent, OH 44242, USA  
Department of Chemistry and Biochemistry, Kent State University, Kent, OH 44242, USA  
Brain Health Research Institute, Kent State University, Kent, OH 44242, USA

\*All co-authors contributed equally to the write-up of this review.

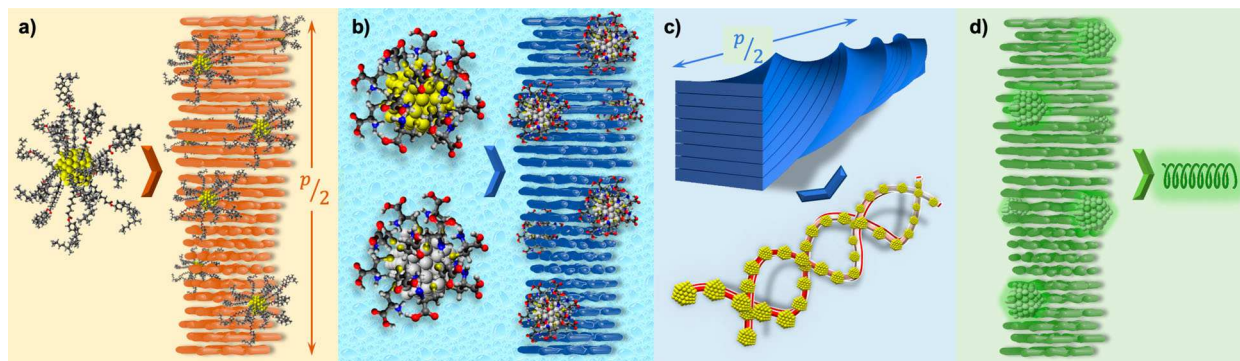


**Figure 1.** Schematic illustration of the approaches discussed in this review: (a) quantifying nanoparticle chirality (here plasmonic nanoparticles with a hydrophobic chiral ligand shell) using induced chiral liquid crystal phases as a reporter (for example by measuring the helical pitch,  $p$ , and calculating the helical twisting power in an induced  $N^*$ -phase) and (b) a similar approach using an induced lyotropic  $N^*$ -LC phase. (c) One of several approaches for the helical assembly of achiral nanoparticles (such as plasmonic nanoparticles with an achiral ligand shell) using a chiral organic nanoscale template (here B4 helical nanofilaments, HNF, formed by bent-core molecules). (d) Chiral assembly of emissive nanomaterials using chiral LC phases for circular polarized luminescence (CPL).

in this area to chiral nanoscale structures and assemblies that mimic, rival or interact with natural chiral systems [19, 20]. Synthesis and nanofabrication as well as chiral assembly strategies continue to bring potential technological use of the resulting chiral nanostructures into close reach. Currently, anticipated front runners are photonic, sensing, catalytic, and medical applications [21]. Considering the similarity in scale, both of the underlying building blocks as well as the supramolecular structures formed by them, liquid crystals should be considered an archetypical platform to detect, measure, and visualize nanomaterial chirality and serve further as highly tuneable hosts to assemble nanostructures in a variety of chiral fashions (spiral, helical) [22–25].

Liquid crystal phases show extraordinary sensitivity to either the introduction of chiral centres into the mesogenic molecules or the admixing of chiral additives [26]. Chiral phase modifications can be induced into their achiral counterparts — the prime pair most frequently studied being the achiral nematic (N) and the induced chiral nematic ( $N^*$ ) phase [27] — and some phase structures exist only when chirality is present (*e.g.* in the case of blue phases [28]); yet others exist in the form of chiral conglomerates even in the absence of molecular chirality as, for example, in the case of the B4 phase formed by some bent-core molecules [29].

This review will attempt to highlight recent research where chirality serves as the interface between nanomaterials and liquid crystals. The aim is not to provide an all-inclusive listing of all the research in this area, but a discussion of the most promising approaches to detect and quantify nanomaterial chirality, attempts to elucidate the role of chirality amplification at the nanoscale, and the use of liquid crystal phases or crystalline modifications formed by mesogenic molecules to template the chiral

assembly of functional nanostructures varying in shape and core material (Figure 1).

## 2. Quantifying nanoparticle chirality

Understanding and controlling the chirality of molecules, nanoparticles and -clusters as well as surfaces is a central theme in various fields of science, from fundamental research on elucidating the origin of homochirality [30, 31] to understanding how chirality transfers across distances and length scales [18]. Homochirality, *i.e.* the single handedness of key biological molecules, is ubiquitous in nature and a key signature of life. Living organisms use virtually exclusively L-amino-acids and D-sugars as building blocks for proteins and nucleic acids. Researchers have invested a great deal of effort to elucidate the origin of homochirality, and chirality amplification, or more accurately, amplified enantioselectivity, emerged as one of several critical underlying concepts [32].

How the sensitivity of LC phases to chiral perturbations can potentially be used to visualize and measure chirality transfer and amplification is the focus of the next section. Several experimental reports highlight that LC phases allow for the visualization of the extent of chirality transfer to a surrounding medium. Furthermore, induced  $N^*$ -LC phases permit a ranking of the chiral induction strength with respect to size, shape, and aspect ratio. Such approaches were based on the experimentally deduced amplification of chirality from chiral nanoscale surfaces dispersed in an LC medium. Here, the induced  $N^*$ -LC phase turns out to be a suitable reporter, presenting characteristic defect texture changes after doping with a chiral nanoscale additives [33]. Initial focus will be on thermotropic LCs as reporters of

chiral induction and amplification, lyotropic LC systems based on either surfactants or chromonic LCs will then be discussed especially for more biological relevant chiral nanomaterials.

## 2.1. Amplification of NP chirality – the thermotropic N\*-LC phase as reporter

### 2.1.1. Polyhedral gold nanoparticles (Au NPs) with chiral ligand shells

Origins of metal and semiconductor NP chirality can, in principle, be divided into four classifications. For any given chiral NP, more than one of them can be active. In these classifications the chirality is associated with: (1) an asymmetry in the core [6–8], (2) an asymmetry of the NP core surface [34], (3) a chiral field effect [35, 36], and (4) an asymmetry of the chiral surface stabilizing molecules (ligand shell) [37]. Each of these have been the subject of intense studies over the past two decades, and for most chiral NP systems the extent and origin of NP chirality in each experimental case is now reasonably well understood. Circular dichroism (CD) spectroscopy (both absorption-based [38] and vibrational CD [39]), single crystal X-ray diffraction [6, 8] as well as theoretical approaches based, for example, on the Hausdorff chirality measure (HCM) [40] are now well established, but do leave open questions: How and how effective does the chirality from chiral NPs transmit to their surrounding? This is where LC phases can play and have played a distinctive role, and the following examples may highlight this.

Figure 2 shows a series of three Au NPs that were used to elucidate the role of NP size as well as the presence or absence of a chiral bias during NP formation (*i.e.* during the NP synthesis) on the chiroptical activity of these chiral ligand capped Au NPs. Experimentally, only NP1 and NP2 visibly induced N\*-LC phases. These two NPs were prepared in the presence of a chiral bias (*i.e.* the chiral cholesterol disulphide using during the NP synthesis); NP3 was formed in the absence of a chiral bias (prepared by conjugation of the cholesterol-siloxane to the preformed 3-mercaptopropylsilane-capped Au NPs). The resulting doped N-LC phase showed no or only limited indication of chirality transfer. This result illustrates that interactions between N-LC phases and chiral ligand-capped Au NPs can serve as a platform to sense and quantify NP chirality. This can be accomplished by using the well-established methods to quantify chirality in induced N\*-LCs such as measuring the helical pitch,  $p$ , and calculating the helical twisting power ( $\beta_w$ ). Measurements of  $p$  in different N-LC hosts underlined a clear dependency on Au NP size and thereby the number of chiral ligands on the NP surface. At a concentration of

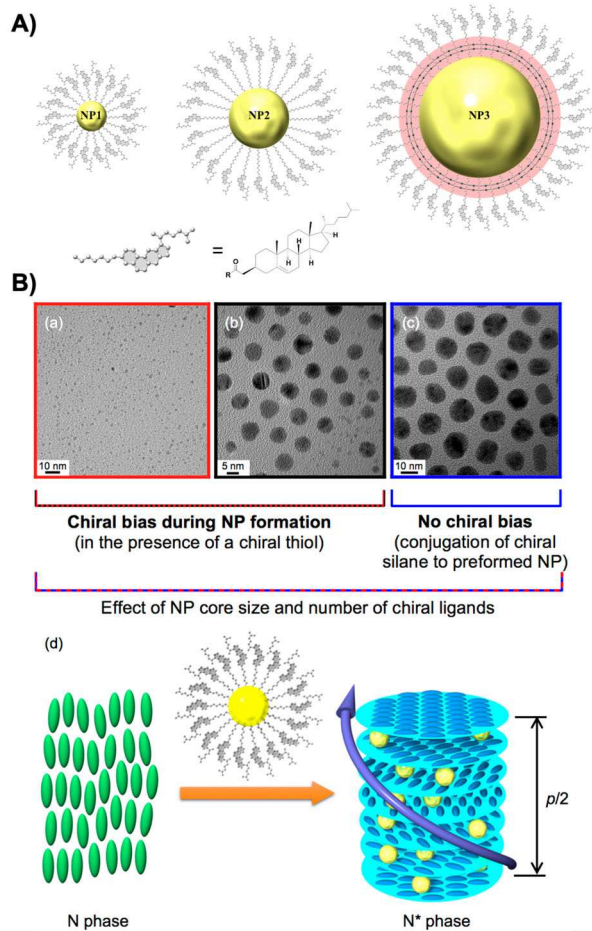


**Figure 2.** (A) Schematics of the Au NPs capped with cholesterols (chiral bias during NP formation: NP1 and NP2) or capped with a cholesterol-siloxane derivative in a subsequent step *via* silane-conjugation (no chiral bias during NP formation). (B) High-resolution TEM images of: (a) NP1 ( $1.8 \pm 0.1$  nm), (b) NP2 ( $5.5 \pm 1.2$  nm), and (c) NP3 ( $10.1 \pm 2.7$  nm). (d) Schematic introducing the concept of using an N-LC phase to detect, visualize, and measure the chirality of chiral ligand-capped Au NPs using measurements of  $p$ . Reproduced with permission from reference [33]- Published by American Chemical Society.

5 wt.%, NP1 and NP2 in 5CB showed characteristic N\*-LC fingerprint textures with values of  $p$  ranging from 5 to 6  $\mu\text{m}$ , however, NP3 showed textures similar to chiral finger textures indicating a significantly larger  $p$  in comparison to NP1 or NP2 in 5CB. For comparison, the free ligands (in the form of disulphides) at the same concentration of 5 wt.% in 5CB induced N\* phases with values of  $p$  similar to NP1 or NP2 (about 4  $\mu\text{m}$ ). These observations confirmed the speculation that Au NPs formed in the presence of a chiral bias are more efficient chiral inducers than NPs formed in absence of a chiral bias as well as the free parent organic chiral additives in N-LC hosts. By comparing the amount of chiral ligand present (*i.e.* standardizing the  $\beta_w$  values based on the number of chiral molecules in each mixture – thus introducing the



molar helical twisting power  $\beta_{\text{mol}}$ ), NP1 and NP2 showed significantly higher values of  $\beta_{\text{mol}}$  than NP3 or the free cholesterol ligands. In fact, they showed similar values of  $p$  despite two to three orders of magnitude fewer chiral molecules.

This first small set of Au NPs taught us initially that smaller NPs with an overall lower number of chiral ligands attached to the NP surface in the N-LC mixture outperformed larger ones and that the chemical origin of chirality matters. The key finding, however, was that Au NP chirality can be transmitted to and sensed by N-LC phases, which, in turn, permitted imaging and measurement of the extent of Au NP chirality transfer [33].

Further extension of this work explored how chirality propagates from Au NPs similar in core diameter to NP1 above and capped with enantiomeric pairs of axially chiral binaphthyl molecules [41]. Another problem addressed in this work was how far chirality from a NP surface reaches into the induced N\*-LC bulk and how molecular conformation of such chiral ligands is altered in the condensed N-LC phase. Circular dichroism (CD) spectra of the Au NPs decorated with these binaphthyl thiols (only differing in the length of the non-tethered aliphatic chain) confirmed that the binaphthyl moieties form a *cisoid* conformation in isotropic organic solvents. In the N\*-LC phase, induced by dispersing the Au NPs, the binaphthyl moieties on the NP surface form a *transoid* conformation as determined by observations of the helical twist direction of the induced N\*-LC phase. This suggests that ligand monolayers on nanoscale metal surfaces provide a dynamic space to alter and adjust the helicity of binaphthyl derivatives in response to the ordering of the surrounding medium (Figure 3). Remarkably, the  $\beta_w$  increased with increasing diameter of the Au NPs from about 1.1–2.5 nm, that is, the efficiency of the chirality transfer of the binaphthyl units bound to the NP surface was diminished as the size of the NP was reduced.

The  $\beta_w$  values for the Au NPs assumed to be a single molecule range from 68 to 376  $\mu\text{m}^{-1}$ , with Au-R1 and Au-R2 showing the highest  $\beta_w$  values of 376 and 371  $\mu\text{m}^{-1}$  for this series (Au-R1 and Au-R2 featuring the larger core diameter values of 2.5 and 2.1 nm for the core diameter, respectively). These  $\beta_w$  values were significantly higher than those calculated for the free ligands and any of the binaphthyl precursors, ranging from 4.0–17  $\mu\text{m}^{-1}$ . Therefore, all Au NPs were considered more efficient chiral additives when compared to the free organic ligands. For example, measured values of  $p$  values of the N\*-LC phases induced by the R2 and Au-R2 pair at the same mole fraction of  $1.4 \times 10^{-2}$  mol% in 5CB were 500  $\mu\text{m}$  for R2 and 19.6  $\mu\text{m}$  for Au-R2 — a 25-times tighter helical pitch induced by the Au NPs. The

$\beta_w$  values for the Au NPs of course depend on the number of the binaphthyl units on the Au NP surface. Hence,  $\beta_w$  values of a single binaphthyl unit on the Au-NP surfaces were calculated and varied from 7.0–14.5  $\mu\text{m}^{-1}$ ; values that are indeed similar to those for the free ligands (9.8  $\mu\text{m}^{-1}$ –16.1  $\mu\text{m}^{-1}$ ). Such comparison is of course flawed: ligands on the NP surface are much less able to fully interact with the surrounding 5CB host molecules. In comparison to the free ligands, again normalized to the number of chiral molecules, all tested Au NPs induced helical distortions in a 10- (for the NPs with smaller core diameter) to 50-fold (for the NPs with larger core diameter) larger number of N-LC host molecules surrounding each Au NP, indicating a significantly enhanced chiral correlation length. Both the helicity and the chirality transfer efficiency of axially chiral binaphthyl derivatives can therefore be controlled at metal NP/N-LC interfaces by adjusting the NP size and curvature as well as the number and density of the chiral ligands to ultimately measure and tune the chiral correlation length (Figure 3c-d).

Overall, this study seemed to suggest that for a given NP shape (here quasi-spherical, polyhedral NPs), a ‘sweet spot’ for the average NP core diameter exists, where the amplification of chirality is maximized; potentially a compromise between the miscibility of the NP in the N-LC, an increasing density of the ligand shell as the core diameter increases, and the collective action of a network of chiral ligand molecules forming a monolayer on the NP surface.

### 2.1.2. Gold nanorods (GNRs) with chiral ligand shells

To further assess the validity of these assumptions and considering that an enhancement of through-space chirality transfer finds support from examples of demonstrated long-range, through-space interactions between chiral molecules and plasmonic nanostructures [36, 42, 43], desymmetrization of quasi-spherical Au NPs to Au nanorods (GNRs) coupled with shape complementarity between the constituents (molecules of the surrounding medium and nanorods) should translate into further increasing  $\beta_w$  values (Figure 4a) [44]. If a correlation between spectroscopic data and experimental  $\beta_w$  data from the induced N\*-LC phases exists, enhanced anisotropy or Kuhn’s dissymmetry factors [45, 46]  $g$  for chiral GNRs ( $g = \Delta\varepsilon/\varepsilon$ , where  $\Delta\varepsilon$  and  $\varepsilon$  are the molar circular dichroism and molar extinction coefficient, respectively) obtained from absorption and CD measurements would further support such assumption.

As it turns out, the values for  $\beta_{\text{mol}}$  reported in this subsequent study for two GNRs capped with the cholesterol-silane shell (shown earlier in Figure 2A) are among the

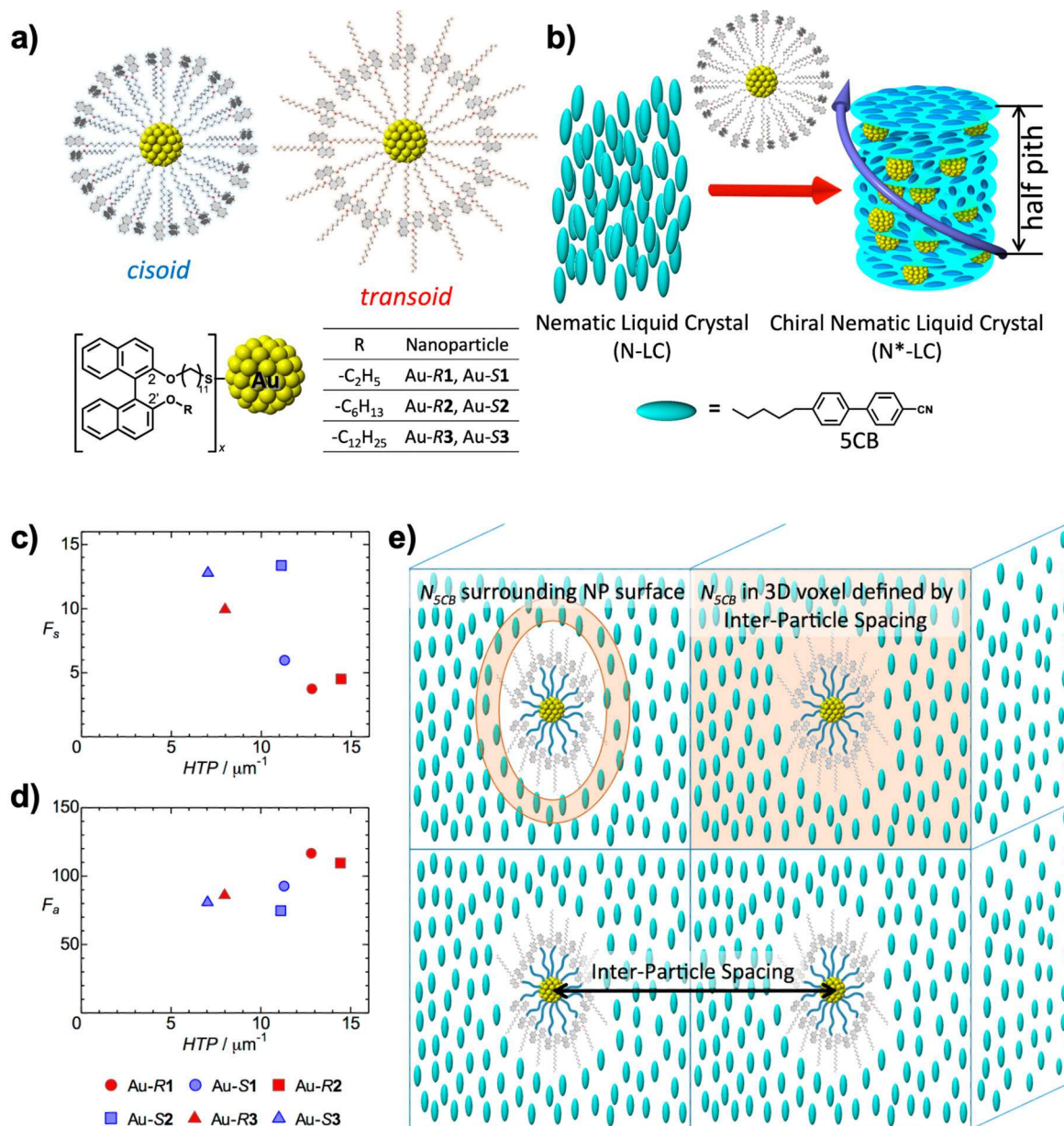


**Figure 3.** (a) Schematic structures of *cisoid* and *transoid* conformations (in solution and in the induced N\*-LC phase, respectively) of binaphthyl derivatives as ligand shells capping the surface of Au NPs and the Au NPs [Au-R1, -R2, and R3 as well as Au-S1, S2, and S3] with undecanoyl thiolate and an alkyloxy chain differing in length [ethyl, hexyl, and dodecyl] at the 2- and 2'-position of the binaphthyl, respectively. (b) N\*-LC phase induced by the addition of the Au-NPs functionalized with chiral binaphthyl moieties. Plots of: (c)  $F_s$  (ratio between the number of 5CB molecules near the Au NP surface/number of binaphthyl molecules on the Au NP surface) vs. HTP ( $\beta_w$ ) and (b)  $F_a$  ratio between the total number of 5CB molecules in a 3D voxel surrounding one Au NP surface/number of binaphthyl molecules on the Au NP surface (*cf.* panel (d)) vs. HTP ( $\beta_w$ ). (d) Schematic 2D representations of 5CB molecules surrounding the Au NP surfaces in the 3D space (voxel) defined by the interparticle distance assuming reasonably well-dispersed Au NPs in the 5CB matrix (for simplicity, the helical distortion of the 5CB molecules in the induced N\*-LC phase is not shown). Reproduced with permission from reference [41] - Published by the American Chemical Society.

highest values reported in the literature to date and the values for  $\beta_{mol}$  are even higher by one, even two orders of magnitude than any prior value reported for even the most potent chiral inducers of N\*-LC phases (Figure 4b) [44].

To see if a cooperative effect is responsible for these high  $\beta_{mol}$  values, *i.e.* if a potential helical distortion of the chiral ligand shell-capped GNRs further enhances this chirality transfer, freeze-fracture TEM (FF-TEM) images of a N\*-LC droplet on glass support were obtained. These

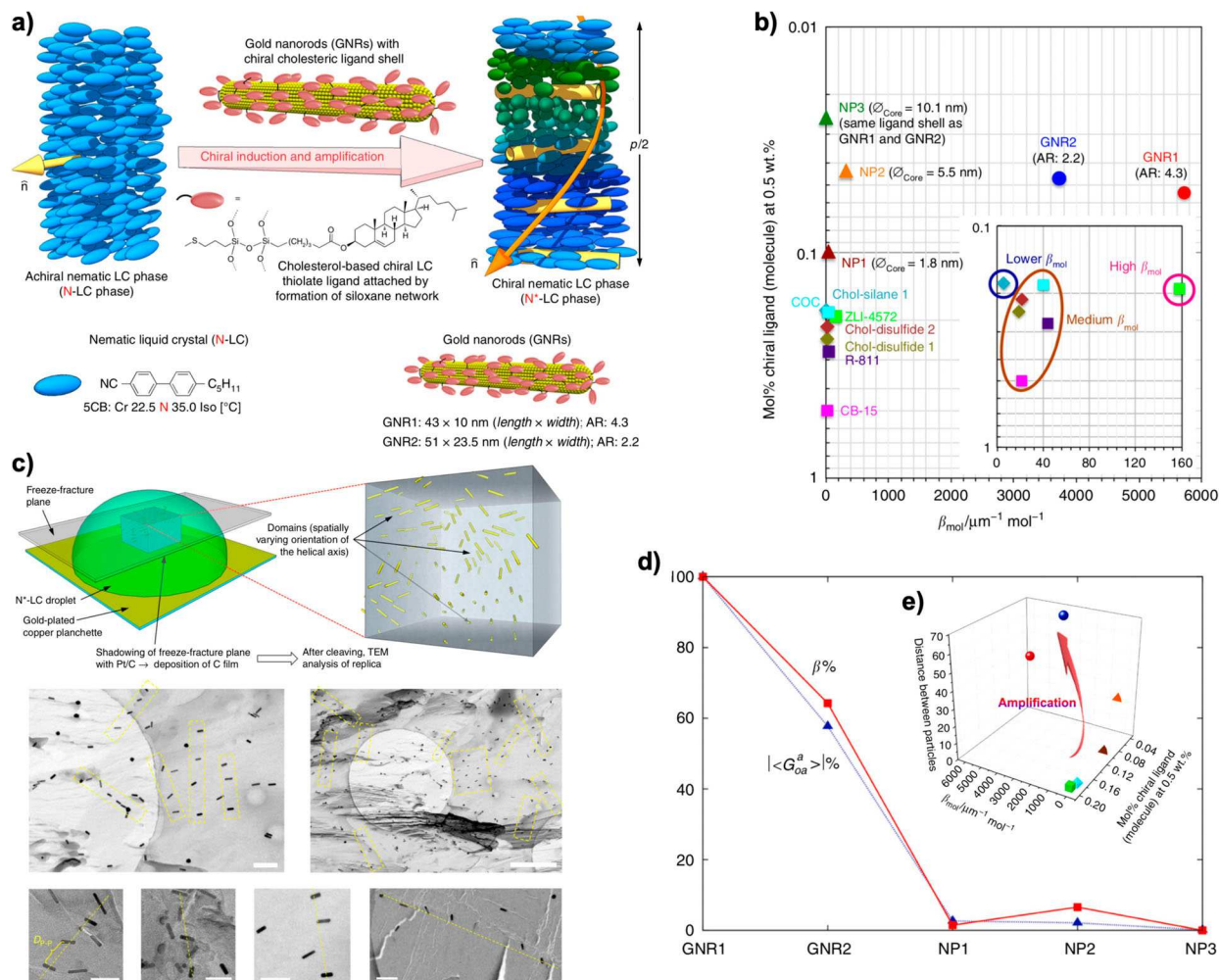


**Figure 4.** (a) Materials and approach to test chiral amplification by desymmetrization: N\*-LC phase induced by addition of minute amounts of chiral cholesterol-capped GNRs into an achiral N-LC host and depiction of dimensions of GNR1 and GNR2. (b) Plot of  $\beta_{mol}$  vs. the concentration (mol fraction, mole%) calculated for 0.5 wt.% of a range of chiral additives (including GNR1 and GNR2, NP1 – NP3 shown in Figure 2, the free cholesterol ligands, and a range of commercial chiral dopants). (c) Approach and images from freeze-fracture TEM analysis of the N\*-LC induced by GNR1. (d) Trend of  $|G_{0a}^a|$  for the GNRs with 20 coarse-grained representations of the cholesterol-silane ligands compared to the experimental trend of  $\beta_{mol}$ . (e) 3D chirality transfer efficiency plot: ( $\beta_{mol}$  vs. concentration) vs.  $D_{p-p}$ . Reproduced with permission from reference [44] - Published by Springer Nature.

imaging experiments confirmed that a GNR helical distortion is self-induced, and further permitted an assessment of the average distance between adjacent GNRs in the induced N\*-LC matrix. This value, the particle-particle distance ( $D_{p-p}$ ), is then again used as the chiral correlation length between neighbouring chiral inducers and serves as a comparable quantity for chirality amplification through space (Figure 4c).

This study further employed an absolute, rather than relative to a reference, pseudoscalar indicator derived from the molecule's (or more generally an object's) geometry. This average chirality index  $|G_{0a}^a|$ , validated and employed for small molecules [47], proteins [48], and cellulose nanocrystals [49], depends only on geometric information, *i.e.* in this case the position and orientation

of the chiral cholesterol ligands with respect to the GNR or NP frame, and thus indirectly on the shape and size of the nanomaterial. As shown in Figure 4d, the trends of the computed  $|G_{0a}^a|$  is in very good agreement with the experimental  $\beta_{mol}$  values considering the two GNRs and the three cholesterol capped Au NPs shown in Figure 2. The variation of chirality with size and shape is reproduced without any fitting parameter. Considering that no specific materials' parameters for the nature of the GNRs or Au NPs was introduced, these results further strongly suggest that the origin of the chiral amplification effect is related to the chiral ligands attached to these nanostructures forming a network (Figure 4e). In this way, the chiral ligand shell acts as a network, thereby augmenting the overall chirality.



The same approach was then used to demonstrate how this amplification of chirality facilitated by the GNRs' anisometric and commensurate shape can be used to distinguish the chiral induction strength of a homologous series of the binaphthyl derivatives already shown in Figure 3, differing only in the length of the nontethered aliphatic hydrocarbon chain (Figure 5a). The combined experimental and calculated  $|G_{oa}^a|$  data show that the chirality amplification effect is sufficiently sensitive to differentiate even these subtle structural effects in the chiral additives with respect to chirality transfer.

Elongation of the aliphatic chains at the 2'-positions of these axially chiral binaphthyl derivatives should lead to an increase in the dihedral angle of the *transoid* conformation when dispersed in the N-LC medium. For the free organic binaphthyl derivatives (*R*)- or (*S*)-1 to (*R*)- or (*S*)-3 this change in dihedral angle appears to be too small to result in detectable changes in  $\beta_{mol}$  considering experimental standard deviations. However, by amplifying chirality transfer through fixation of these binaphthyl derivatives onto GNRs such anticipated minor changes in the dihedral angle can now be detected with great precision and certainty (Figure 5b-d)[50].

A related strategy was then also pursued by Mehl and co-workers, where the Au NPs were simultaneously capped with aliphatic, mesogenic as well as axially chiral binaphthyl thiol ligands. This combination contributes to a 'domino/sergeant-soldier effect' effect, which is introduced to explain the even higher  $\beta_{mol}$  values achieved for these Au NPs in 5CB. Here, the additional introduction of the mesogenic groups to the surface of the mixed ligand shell Au NPs further enhances the miscibility and compatibility of the Au NPs with the N-LC host matrix best supported by arguments of solute-solvent interactions (Figure 6A)[51]. Furthermore, combinations of aliphatic and chiral mesogenic ligands on Au NP surfaces can lead to chiral (helical) NP superstructures (oblique 2D lattices) as demonstrated using grazing incidence small-angle X-ray scattering (GI-SAXS) as well as synchrotron radiation-based CD experiments (Figure 6B)[52]. Similar design strategies involving cholesterol functionalized arylamine-capped Au NPs have led to the discovery of chiral (helically-twisted) lamellar superstructure [53, 54].

To apply this amplification of chirality bestowed by the immobilization of chiral molecules on Au NP surfaces, a recent study demonstrated how chiral ligand-capped Au NPs influence an N\*-LC-based converging microlens array [55]. Creating a microlens array commonly requires often complex micro- or nanofabrication procedures. Flat birefringent lenses such as Pancharatnam-Berry (PB) phase microlenses can provide spatially varying optical axes in the plane normal to the light. Suspending

an N\*-LC mixture in micron-size TEM grids enables the spontaneous formation of biconvex lenses when immersed under water; the degenerate planar anchoring created by the immersion under water rotates the director radially as the thickness changes, similar to Pancharatnam-Berry (PB) phase microlenses. Using this rather simple method, the curvature radius of the N\*-LC lens is proportional to the helical pitch, which is now favourably and predictably tuneable using chiral ligand-capped Au NPs as strong inducers. Furthermore, the lens architecture is suitable to measure  $p$  with suitable precision using only nanogram of strong chiral inducers such as the Au NPs used in these experiments with a core diameter of  $d = 3$  nm capped with a cholesterol-thiol ligand and shell (Figure 7). This rather tiny amount is about three orders of magnitude less than the usual quantity required by conventional techniques, and the NPs are responsive to external stimuli such as electric or magnetic fields as well as and lights (depending on the nature of the core material), which bodes well for the development of highly tuneable optical properties for such microlens arrays [55].

## 2.2. Amplification of NP chirality – lyotropic LC phases

Similar to the use of thermotropic N-LCs to ascertain chirality amplification of nanomaterials with hydrophobic chiral ligand shells, lyotropic LC phases (both chiral and achiral lyotropic nematic phases) have served as matrices to study nanomaterial chirality and helical assembly of nanomaterials with more hydrophilic ligand shells. While more relevant for a better understanding of the chirality transfer and amplification of biologically relevant chiral molecules, research on these systems is additionally complicated by the fact that the extra component, *i.e.* the use of a solvent (predominantly water), leads to ternary mixtures, where both the solvent and the molecules (or aggregates of molecules) forming the mesogenic structure compete in solubilizing the dispersed nanomaterial. Three particularly relevant systems will be discussed in this section: cellulose nanocrystals (CNCs), lyotropic chromonic LCs (LCLCs), and DNA nanostructures.

### 2.2.1. Cellulose nanocrystals - CNCs

Cellulose is the one of the most plentiful polymers and an example of sophisticated hierarchical structure formation in nature. Billions of tons of cellulose are produced every year [56]. The main source of it is trees and plants, however, it can be obtained from different organisms such as fungi or bacteria as well [57]. As a chiral pool material, cellulose is a renewable, nontoxic and low-cost natural

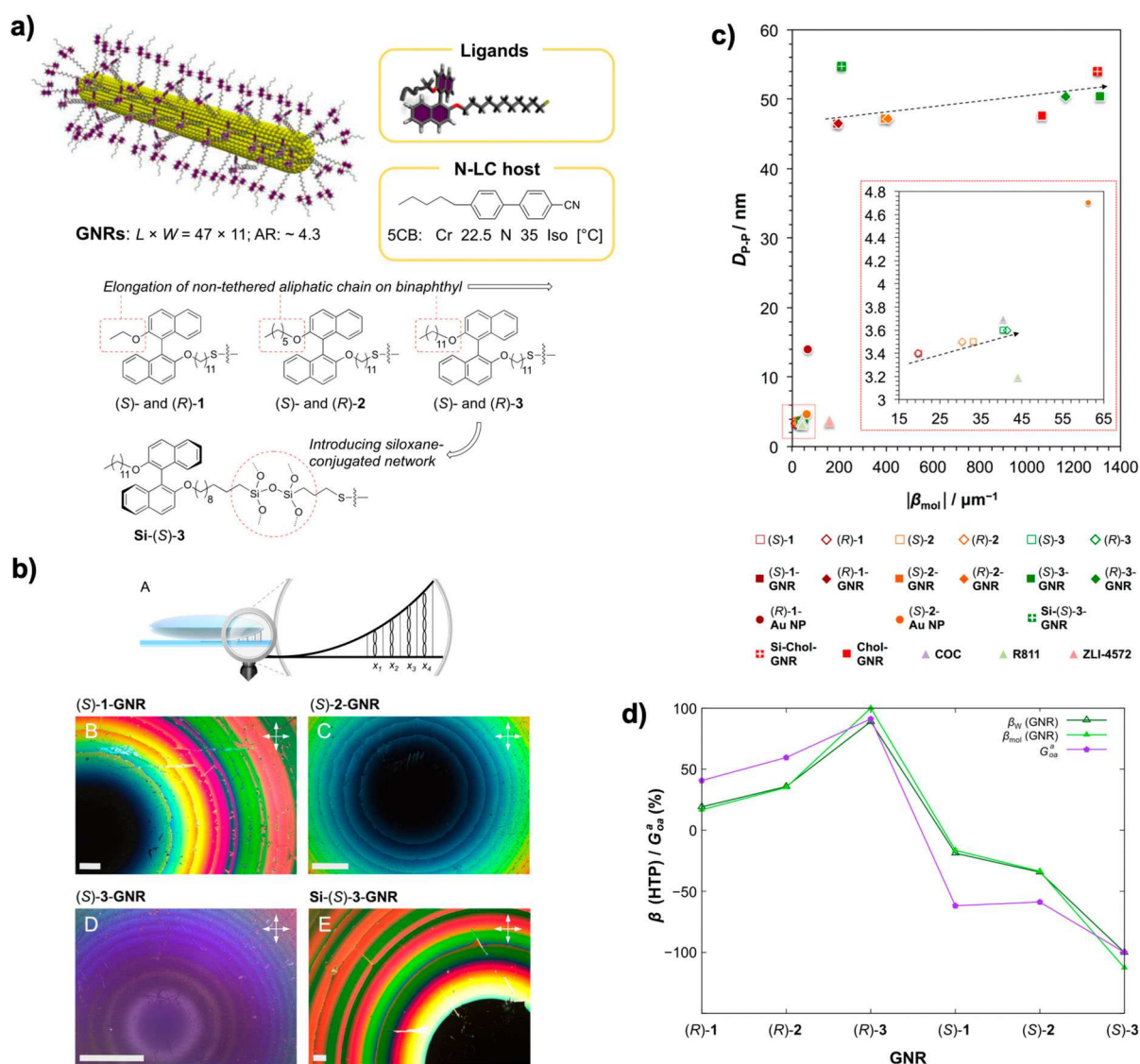


**Figure 5.** (a) GNRs with axially chiral binaphthyl ligands differing in the length of the nontethered aliphatic chain in the 2'-position. (b) Aside from measuring  $p$  using methods such as free surface (top interface is air) and preparation favouring homeotropic anchoring at both substrates, Grandjean–Cano lens experiments were used to determine  $p$  using a plano-convex lens on flat glass substrate both treated with rubbed polyimide to induce planar anchoring (A) method, (B–E) photomicrographs (crossed polarizer). (c) Chirality efficiency plot:  $D_{P-P}$  vs.  $|\beta_{\text{mol}}|$  for the binaphthyl-thiol capped GNRs as well as the free ligands (inset), commercially available chiral dopants, and cholesterol-thiol as well as cholesterol-siloxane shell capped GNRs (see legend beneath plot). (d) Trend of  $|\beta_{\text{HTP}} / G_{\text{OA}}^a|$  for the six GNRs compared to the experimental trends of  $\beta_w$  and  $\beta_{\text{mol}}$ . Reproduced with permission from reference [50] - Published by the American Chemical Society.

source and in increasingly demand as a functional material. Used predominantly in the pulp and paper industry, the reason for this is the discovery that when undergoing mechanical and chemical treatments (such as hydrolysis with mineral acids) one obtains rod like nanocrystals which (cellulose nanocrystals or CNCs) by breaking the amorphous parts of cellulose and releasing individual crystalline parts of it [58]. The source of cellulose, reaction time, temperature, and the type of acid treatment (such as sulfuric, hydrochloric or phosphoric acid) alter

the size of the CNCs, typically ranging from 50 to 1160 nm in length and 3–50 nm in diameter [59, 60]. The most commonly used sulfuric acid treatment creates CNC colloidal dispersions with good colloidal stability due to the negatively charged surface created by the conversion of surface hydroxyl groups into sulphate ester groups that stabilize the colloidal suspensions by electrostatic repulsion in aqueous dispersion [61, 62]. Figure 8 illustrates this acid treatment of wood/tree pulp for the preparation of CNCs.



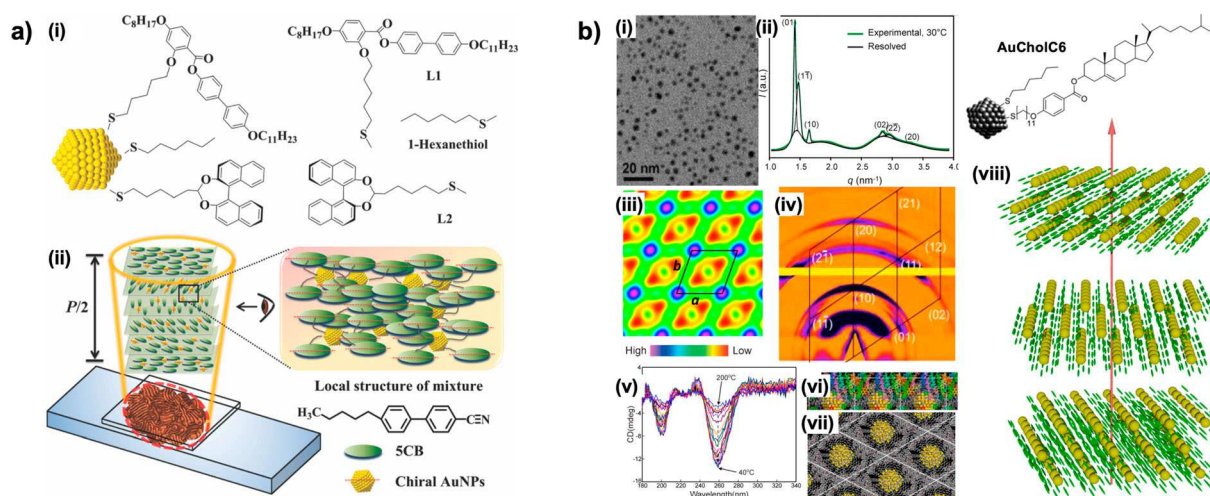


**Figure 6.** (a) Chirality amplification by mixed ligand shell Au NPs: (i) chemical structure of the ligands forming the monolayer capping on the Au NP surface and (ii) schematic showing the induced N\*-LC phase. Reproduced with permission from reference [51] - Published by The Royal Society of Chemistry. (b) Assembly into helical superstructures: (i) TEM image of AuCholC6. (ii) SAXS pattern of annealed AuCholC6 at 30 °C, (iii) electron density map perpendicular to the columns based on intensities of the SAXS reflections in (ii), (iv) GI-SAXS pattern of a slowly cooled thin film of AuCholC6 in the formed mesophase with reciprocal net superimposed, (v) CD spectra of a thin film of AuCholC6 recorded every 10 °C upon cooling from the isotropic liquid phase at 200 °C to 40 °C (the largest increase in ellipticity between 160 and 150 °C coincides with the Iso–2D columnar transition), (vi and vii) show the side and top views, respectively, of a model of several unit cells of AuCholC6 after molecular dynamics annealing, and (viii) schematic representation of the chiral columnar LC phase formed by AuCholC6. Reproduced with permission from reference [52] - Published by the American Chemical Society.

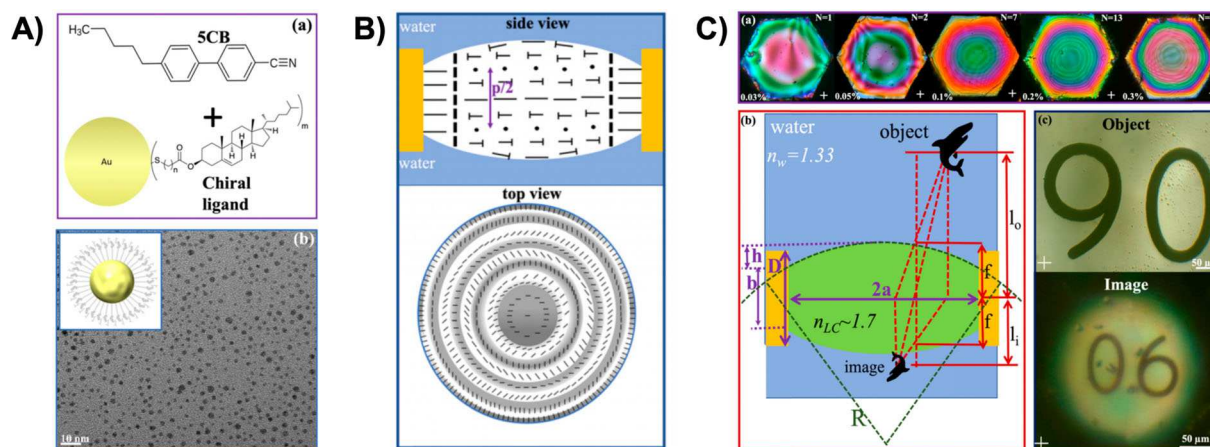


**Figure 7.** Converging microlens array: (A) an N-LC here (a) 5CB doped with cholesterol-thiol-capped Au NPs of  $\sim 3$  nm core diameter (see TEM image in (b)). (B) Side and top views of the director configuration of the N\*-LC in the lens shaped droplets (director rotates both along the film thickness and radially away from the centre of the lens). (C) Illustration of the optics of Au NP-doped N\*-LC lenses: (a) POM images of lenses with concentrations ranging from 0.03 and 0.3 wt.% of the chiral Au NPs numbers at bottom-left and top-right show the concentration and the number of fringes, respectively. (b) Optical ray tracing of the biconvex LC lens and the geometry of the lens. (c) Images of the object (# '90') and its inverted image at 0.2 wt.% Au NP N\*-LC lens. Reproduced with permission from reference [55] - Published by the American Chemical Society.

Since their discovery, CNCs are used as reinforcement materials in food [63], polymer [64, 65], and pharmaceutical industries [66]. However, more relevant for soft matter materials science has been the discovery that aqueous dispersions of CNCs form a lyotropic N\*-LC phases and that the ensuing left-handed N\* ordering is maintained in solid films created by evaporation-induced self-assembly (EISA) [67–70]. The helical pitch,  $p$ , of the dried films

ranges from microns down to submicrons, giving rise to iridescence colour as a result of Bragg reflection of visible light due to the photonic band gap (PBG), which is the most characteristic physical parameter for one-dimensional photonic crystals and obeys Bragg's law (Eq. 1): [71]

$$\lambda_{PBG} = n p \sin\theta \quad (1)$$

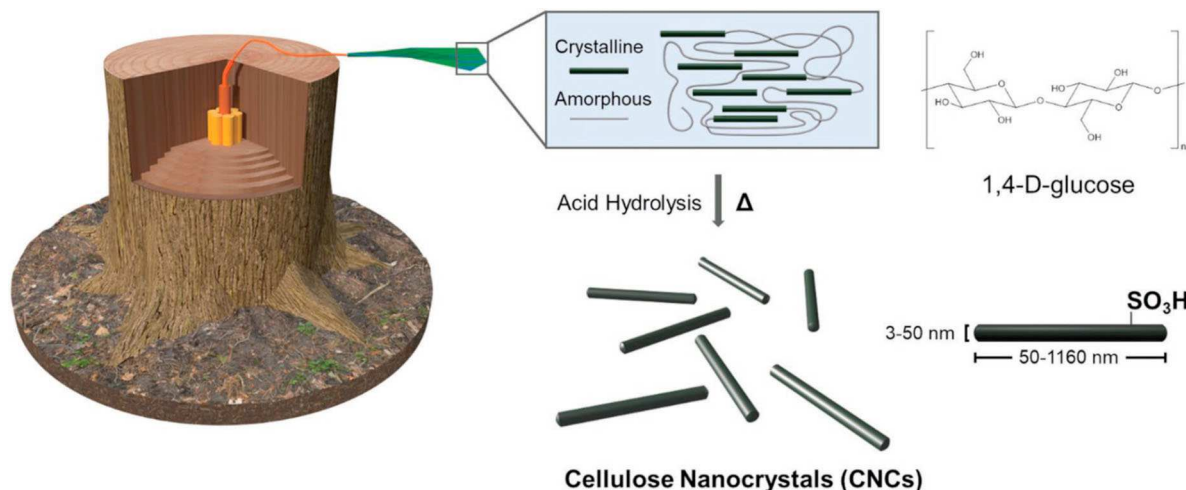


**Figure 8.** Production of CNCs from wood sources using acid hydrolysis treatment. Image is obtained with permission from reference [60] - Copyright 2020 WILEY-VCH Verlag GmbH & Co. KGaA, Weinheim.

where  $n$  is the refractive index of CNC films,  $p$  is the helical pitch, and  $\theta$  the angle of incident light. These features combined with the properties of a photonic crystal and strong circular dichroism (CD), have made CNC films attractive materials for applications in optical devices and, particularly relevant in this review, as chiral templates [72–75]. Representative reports revealed that CNC films are suitable chiral host for the chirality transfer or helical assembly of GNRs, Au NPs as well as semiconductor quantum dots (QDs) resulting in chiral composites for a variety of applications.

Kumacheva *et al.* reported several studies of the effects of various NPs on the structure and optical properties of CNC films: Querejeta-Fernández *et al.* [76], demonstrated that composite films of GNRs and CNCs can result to tuneable chiroptical properties introduced by the plasmonic properties of the GNRs in the  $N^*$  matrix of the CNCs. The group created chiral plasmonic films by admixing GNRs to an aqueous dispersion of 2.44 wt.% CNCs in water and casting films to study the plasmonic chiroptical activity of the GNRs in the  $N^*$ -LC structure and the interaction between the negatively charged CNCs and the positively charged GNRs as a result of the CTAB stabilization of the GNRs assembly in the CNC-water host. Figure 9 depicts the chiral co-assembly of the CNCs and GNRs.

The aqueous suspension was comprised of CNCs with dimensions of 100–200 nm in length and about 17 nm in diameter as well as GNRs with an aspect ratio of  $\sim 3$  (41 and 14 nm an average length and diameter, respectively). Various CNC/GNR ratios (by weight) were prepared by varying the GNR concentrations to create solid films; the observed composite films changed colour to dark red (plasmonic absorption band) with increasing GNR content. Figure 10 shows a selection of cross-sectional

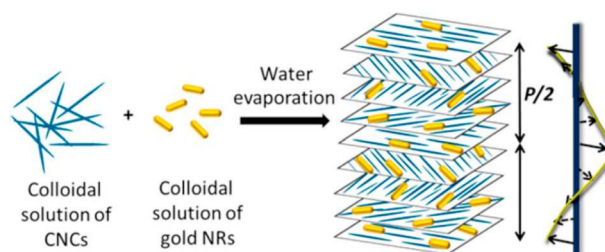


**Figure 9.** Schematic illustration of the CNC/H<sub>2</sub>O + GNRs preparation and the ensuing  $N^*$  assembly of the GNR-CNC hybrid film. Reprinted with permission from reference [76] - Copyright (2014) American Chemical Society.

SEM images of the different GNR concentrations in the CNC films as well as extinction and corresponding CD spectra. Increasing the concentration of GNRs decreased the spacing in the pseudo-layer structure of the CNC films corresponding to a decrease in  $p$ . Furthermore, the extinction spectra of these hybrid films showed two plasmonic bands that red-shifted in comparison to bands observed for the GNRs in aqueous solution (512 and 714 nm) likely due to a change of the surrounding dielectric from water to CNC/water; the intensity of these bands also increased by elevating the concentration of the GNRs. In the CD spectra, bands recorded for the composite films showed a blue shift compared to neat CNC films as a result of the decreasing  $p$  value with successively elevated concentrations of the GNRs.

In the second part of this study, the authors report on a red shift of the GNRs' plasmonic resonance bands when the aspect ratio of the GNRs was increased from 2.4–3 to 4. Similarly, the CD bands again displayed a blue shift. Lastly, at a constant concentration of the suspended GNRs,  $p$  could be tuned by adding NaCl as evidenced by

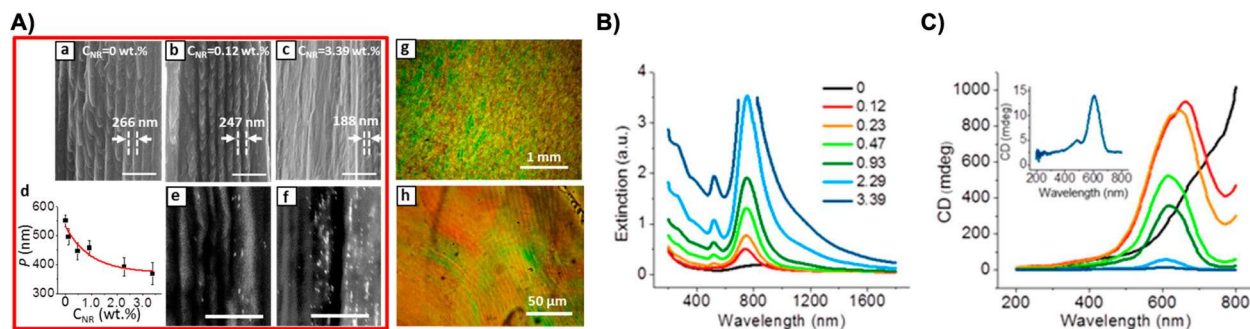


**Figure 10.** (A) Cross-sectional SEM images of GNR/CNC films at GNR concentrations of (a) 0, (b) 0.12 (c) 3.39 wt.% (distances between dashed lines represent  $p/2$ ), (d) plot of  $p$  vs. GNR concentration, (e and f) cross-sectional SEM images of composite films with backscattered electron detector to visualize the GNRs (scale bars: 1  $\mu\text{m}$ ) and (g and h) low- and high-magnification polarization optical microscopy images of the GNR/NC film at  $C_{\text{GNR}} = 0.47$  wt.%. (B) Extinction and (C) CD spectra of hybrid films with different wt.% GNRs (see legend); insert shows a rescaled plot of the CD spectrum of the highest concentration of the GNR (3.39 wt.%). Reprinted and adapted with permission from reference [76]. Copyright (2014) American Chemical Society.

a blue shift of the CD band (increase in  $p$ ) due to electrostatic repulsion between the CNCs. A concentration of NaCl of 2.13 wt.% finally gave rise to the disappearance of the stop band due to the disruption of helical structure.

In a follow up study, Kumacheva and co-workers [77] studied the effects of surface charge, size, and concentration of Au NPs on the optical properties of CNC films. The Au NP dimensions (diameters) were chosen to be smaller or larger than average diameter of the CNCs ( $\sim 13$  nm). Average diameters of 9 and 43 nm of positively charged and negatively surface ligand charged Au NPs were used and their concentration varied from  $10^{12}$  to  $10^{16}$  Au NPs per  $\text{cm}^3$  in a 2.67 wt.% aqueous suspension of CNCs casted as composite films. The results of their experiments showed that altering the size of the Au NPs had less effect than altering the concentration. Extinction spectra of neat CNC films showed a band over a broad spectral range centred at 780 nm and a surface plasmon bands originating from the 9 and 43 nm diameter Au NPs centred at 532 and 545 nm, respectively. Figure 11 shows both the extinction and the CD spectra for the composite films containing the Au NPs differing in size and their concentration. The lowest concentration of either size of Au NPs in the CNC composites showed a peak only at the photonic band gap of the CNC matrix around 713 and 711 nm for both the 9 and 43 nm diameter Au NPs, respectively; similarly, the highest concentration of Au NPs for either size only showed SPR (surface plasmon resonance) bands of the Au NPs.

However, the thin films CD spectra of the hybrid films with lowest Au NP concentrations showed high intensity peaks from 420 to 760 nm, *i.e.* at lower wavelength than for the neat CNC films at 800 nm. Thus, increasing the concentration decreased the intensity of the CD signal as

a result of the interruption of the helical structure already indicated by SEM and POM images. Repeating these experiments for different concentrations of the 43 nm in diameter Au NPs with negatively surface resulted in similar extinction spectra; CD signals on the other hand showed bands that shifted to lower wavelength compared to the positively charged Au NPs.

This study elegantly showed that the concentration of Au NPs affects the optical properties of CNC films. The cholesteric order was influenced, causing a blue shift due to changed ionic strength in the mixture, for both negatively and positively surface charged Au NPs, and at a certain concentration both the CNC films' photonic gap and the SPR band of the Au NPs can be detected concurrently; likewise, a splitting of the CD signals was discussed as a result of induced CD (ICD) activity of the Au NPs.

In addition to plasmonic nanostructures, CNC films have also been examined as a matrix to study excited state chirality using circular polarized luminescence (CPL) measurements. CNC films can serve as tuneable CPL hosts because of their adjustable PBG when doped (or used as a host) for luminescent nanostructures yielding high values of the dissymmetry factor,  $g_{\text{lum}}$  (more details in Section 3.1.1) [78, 79].

Li *et al.* [80], for example, studied combining  $\text{NaYF}_4:\text{TmYb}$  upconverting nanoparticles (UCNPs) (near infrared, NIR, light conversion to UV-visible), which emit at multiple wavelengths and allow for tuning of  $g_{\text{lum}}$  (or CPL) by altering the PBG of the CNC films by adding glycerol. While other studies already reported that adding an increasing amount of glycerol to aqueous CNC suspensions and cast as films (by EISA) shifts the maximum wavelength of the band in the reflection spectra from 400 nm (no glycerol) to 800 nm (50% glycerol ratio) due to increase of  $p$  in the composite films [81], here, the



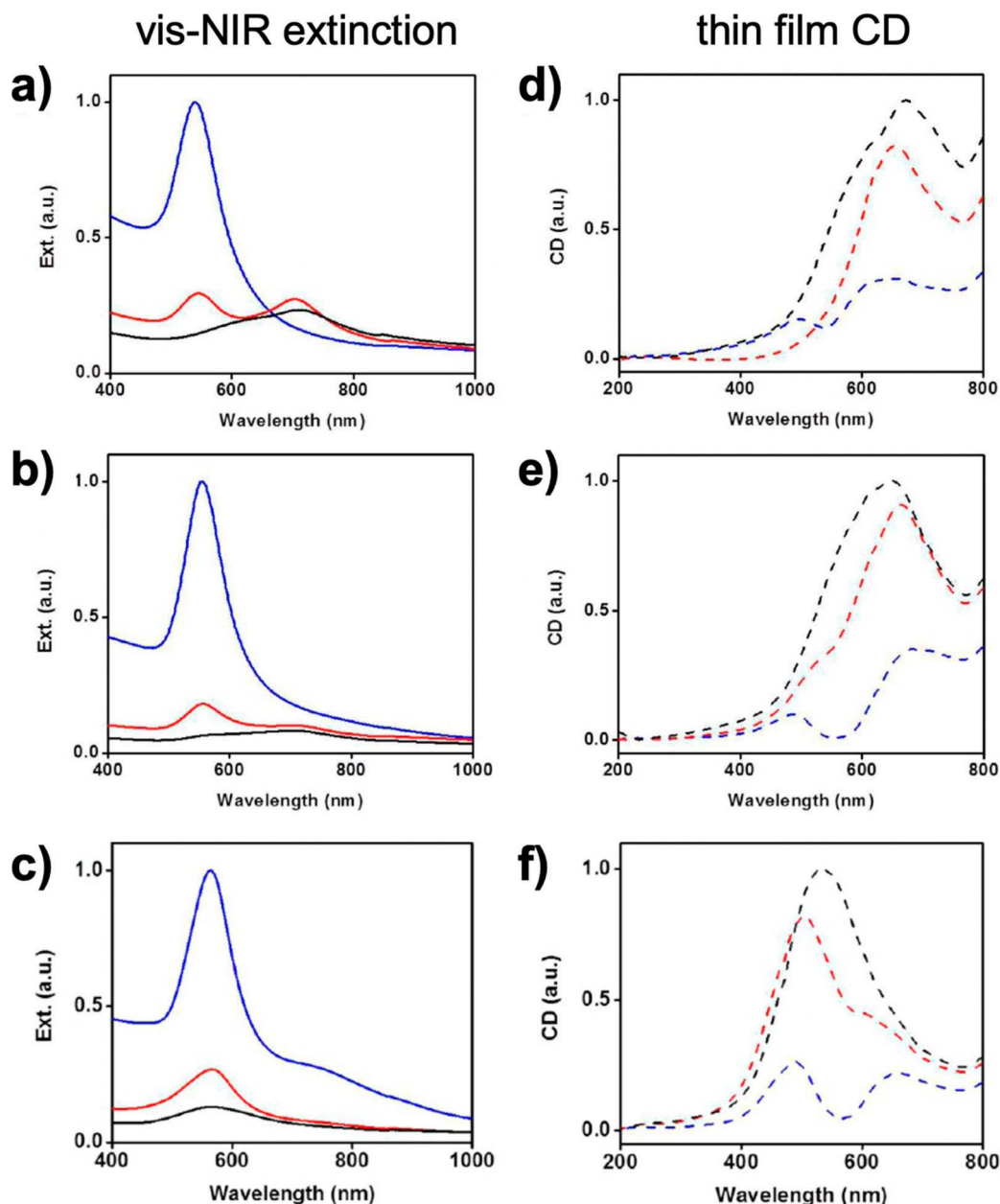


**Figure 11.** Extinction and corresponding CD spectra of the composite films of CNCs with admixed Au NPs: (a and d) (+)AuNPs-9 [labelling: (surface charge)AuNP-core diameter in nm] at varying concentrations of the Au NPs of  $10^{13}$  (black traces),  $10^{15}$  (red traces), and  $10^{16}$  (blue traces) Au NPs per  $\text{cm}^3$ , (b and e) (+)AuNPs-43 at  $10^{12}$  (black traces),  $10^{13}$  (red traces), and  $10^{14}$  (blue traces) Au NPs per  $\text{cm}^3$ , and (c and f) (-)AuNP-43 at  $10^{12}$  (black traces),  $10^{13}$  (red traces), and  $10^{14}$  (blue traces) Au NPs per  $\text{cm}^3$ . Reprinted and adapted with permission from [77] - Copyright (2015) American Chemical Society.

addition of UCNPs and glycerol made the CPL emission susceptible to humidity, thereby enabling UC-CPL as a sensor for changes in humidity Figure 12.

Thin film CD spectra of these films showed intense positive signals, which arises from the left-handed chirality of the CNC films, and the peak wavelength red-shifted with increasing the amount of glycerol (from 410 nm for no glycerol to 638 nm at the highest glycerol content). This further supports why all interrogated

photonic films selectively reflected left-handed CPL (L-CPL). CPL measurements with the films excited at 974 nm in the NIR produced CPL transmission in the visible (right-handed UC-CPL emission peaks) with  $g_{lum}$  values at 450 nm ranging from 0.038–0.019 and at 620 nm from 0.021–0.071 for CNC-U, G1-U and G2-U, respectively. Hence, the three films showed different values for each peak wavelength. To explain this, the authors argued that the  $g_{lum}$  values at 450 nm were greater because

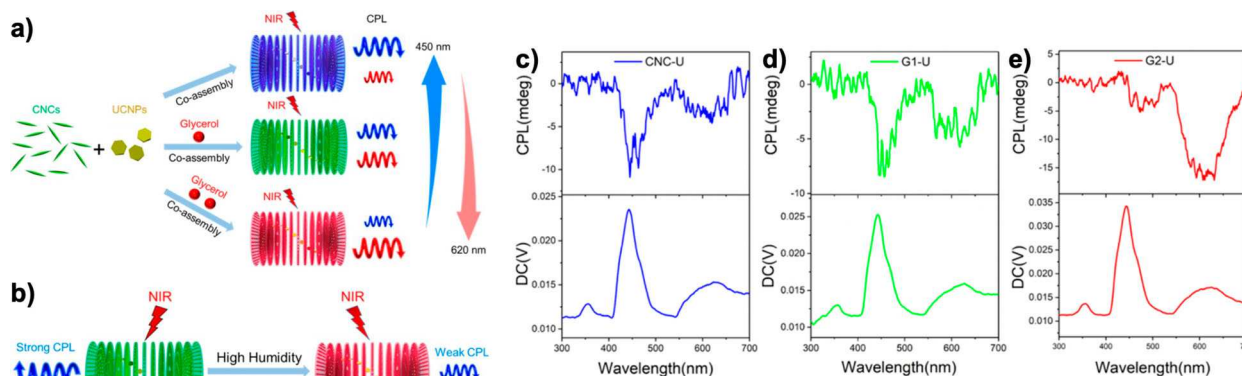


**Figure 12.** (a) Schematic illustration of the prepared CNC-UCNPs films with different concentration of glycerol resulting in tuneable UC-CPL emissions, (b) humidity responsive UC-CPL emission. (c – e) CPL and DC spectra of composite films: (c) CNC-U (glycerol, 0 g), (d) G1-U (glycerol, 0.02 g), and (e) G2-U (glycerol, 0.04 g). Reprinted and adapted with permission from [80] - Copyright (2019) American Chemical Society.

selective chiral amplification *via* the PBG effect in these photonic crystals did not allow L-CPL emission even though the fluorescence emission was overlapped. At 620 nm, however, it was smaller because of the upconverted fluorescence was far away from the PBG. The combined data confirm that CPL emission and  $g_{lum}$  can be tailored more so by the CNC host than the UCNP admixed NPs [81].

In a related set of experiments, Xion *et al.* [82] demonstrated the assembly of carbon QD (CQD) in CNC suspensions as well as the effect of this assembly on their chiroptical and fluorescence properties. Here, suspension of PEG-stabilized CQDs and CNCs formed a core/shell nanostructure. QCD/CNC film exhibited a higher photoluminescence intensity (PL) compared to neat QCD or CNC films, thereby validating that the helical assembly in CNC films as a template enhances fluorescent emission by further limiting QCD aggregation. Values for  $g_{lum}$  reached  $-0.2$  (right-handed fluorescence of the CNC/QCD films due to the left-handed chiral organization of the CNC film). Similarly, Xu and co-workers [83] reported that chiral photonic films composed of CNC, poly(vinyl alcohol) (PVA) and carbon dots (CDs), exhibited tuneable photonic band gaps and tuneable CPL with inverted handedness as well as high  $g_{lum}$  values up to  $(-0.27)$ .

The reader is referred to a number of reviews on the chemistry, self-assembly and on inorganic/CNC hybrid systems [84, 85]. CNCs can be used to helically assemble a wide range of NPs and chromophores in hybrid films and allow the manipulation of CPL properties by acting as a one-dimensional chiral photonic crystal with a  $N^*$  order. The combined photonic and chiral properties of CNCs and the addition of nanostructures with chiroptical properties makes these composite material attractive candidates for biosensing [86],

photoelectronics [87], nonlinear optics [88], and even asymmetric catalysis [89].

### 2.2.2. Lyotropic chromonic LCs - LCLCs

Lyotropic LCs (LLCs) are formed by assemblies or aggregates of amphiphilic molecules in solution. Archetypal LLCs are made from surfactants such as sodium dodecyl sulphate (SDS) or cetyltrimethylammonium bromide (CTAB), which form aggregates such as micelles, vesicles, bilayers, etc., which then form the building blocks of the LC phases [90–92]. However, the building blocks for lyotropic chromonic liquid crystals (LCLCs) are elongated assemblies of plank-like molecules such as the dye, sunset yellow FCF (SSY) or the antihistamine, disodium cromoglycate (DSCG), among others [93–95]. Also included in the LCLC classification are nucleic acids, where LC phases are formed by single- or double-stranded oligomers [96, 97]. LLCs such as cellulose nanocrystals (CNC) [67], described in the preceding section, and other colloidal suspensions such as tobacco mosaic virus (TMV) and inorganic LLCs [98–100] do not fall neatly into the above two categories. While a variety of LC phases are possible (*e.g.* cubic, lamellar –  $L_\alpha$ , columnar – M, etc.), the lyotropic nematic (N) phase is the most relevant for the purposes of chirality detection, transfer, or amplification. As in thermotropic systems, the chiral lyotropic nematic ( $N^*$ ) phase can be attained either by using chiral molecules (*e.g.* chiral co-surfactants for LLCs, or chiral ‘mesogens’ for LCLCs), or by admixing small amounts of chiral guest molecules. This section will focus only on LCLCs and how chirality transfer and amplification have been characterized and quantified upon addition of chiral plasmonic NPs or nanoclusters.

LLCs in general are notorious for their small twist elastic constant,  $K_{22}$ , ( $\sim$  one order of magnitude smaller) compared to the splay and bend elastic constants ( $K_{11}$

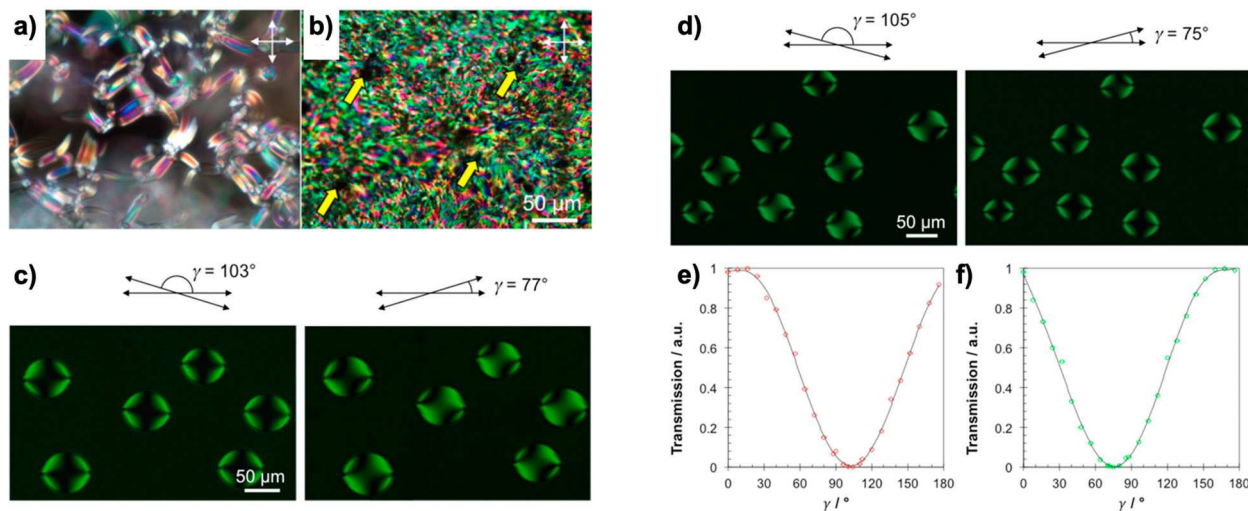


**Figure 13.** POM images of samples at room temperature of DSCG ( $\sim 15$  wt.% in  $\text{H}_2\text{O}$ ) doped with: (a) AMP and (b) AMP-Au NCs at 7 wt.% each. Photomicrographs (c) and (d) represent tactoids at  $37.5$  °C for samples doped with 0.5 wt.% each of AMP and AMP-AuNC, respectively (in the presence of 0.8 wt.% PEG) on cooling from the isotropic liquid phase. For AMP, the transmission through the centres of the tactoids is lowest when  $\gamma = 103 \pm 1^\circ$ , and for the AMP-AuNCs it is when  $\gamma = 75 \pm 1^\circ$ . The experimental data points (empty circles) in (e) and (f) represent the transmission through the centre of the tactoids at different values of  $\gamma$  for AMP- and AMP-AuNC-doped tactoids, respectively – the data are fitted to Eq. 2, and the lines of fit are indicated by the solid lines. Reprinted with permission from [109] - Copyright (2019) American Chemical Society; <https://pubs.acs.org/doi/10.1021/acsomega.8b03335>.

and  $K_{33}$ , respectively) [101–105]. The reason for this is, ostensibly, because of the flexibility of the polymer-like assemblies which can tolerate fluctuations better than molecules (as is the case in thermotropic N-LCs) [101]. One of the implications of such low  $K_{22}$  is that twist deformations are substantially more likely to occur because they are energetically less costly than splay and bend deformations [101]. So, when achiral N-phase LCs are under confinement, spontaneous symmetry breaking may be observed [67, 93–96, 98–100, 106, 107]. Lavrentovich *et al.* demonstrated this phenomenon for an LCLC – disodium cromoglycate (DSCG), to which they added polyethylene glycol (PEG) as a crowding agent, resulting in a racemic mixture of stable nematic droplets (also known as tactoids) in coexistence with the isotropic phase (the concentrations are 14.8 and 0.8 wt.% for DSCG and PEG, respectively) [105].

Textures observed for the condensed phases of DSCG in  $\text{H}_2\text{O}$  (at  $\sim 15$  wt.% and  $20$  °C; bulk phase) doped with 7 wt.% adenosine monophosphate (AMP, Figure 13a) – a biologically relevant nucleotide – as well as with 7 wt.% AMP-capped Au nanoclusters (AMP-Au NCs, Figure 13b) do not convey chirality transfer but show the induction of the columnar phase and aggregation of the NCs, respectively. Figure 13c and d, however, show the appearance of the tactoids (at  $37.5$  °C; biphasic regime) after doping with 0.5 wt.% AMP and AMP-Au NCs observed by polarized optical microscopy. The angle by which the director is twisted,  $\tau$ , is determined by measuring

the transmission of light (described by Eq. 2) through the centre of the tactoid [105, 108, 109] – the magnitude of  $\tau$  is the same for identical tactoids of opposite handedness. Typical transmission curves are shown in Figure 13e and f.

$$T = \cos^2 \beta - \left( \frac{\tau}{2\delta} \right) \sin 2\delta \cos 2\beta \left[ \left( \frac{\tau}{\delta} \right) \tan \delta + \tan 2\beta \right] \quad (2)$$

where  $\delta = \sqrt{\tau^2 + \left( \frac{\pi \Delta n d}{\lambda} \right)^2}$ ,  $\Delta n$  is the birefringence,  $d$  is the depth of the tactoid,  $\beta = \gamma - \tau$ ,  $\gamma$  (is the angle between the polarizer and analyser), and  $\lambda$  is the wavelength of the illuminating light. The optical activity,  $\eta$ , of the tactoid is then approximated using  $\tau: \eta \approx \frac{|\tau|}{c \times d}$ , where  $c$  is the concentration of the chiral additive [108, 109]. Further work from the same group shows that the tactoids can be biased towards one handedness using chiral additives, providing a basis for distinguishing between enantiomers; [19] the subsequent increase in the amount of twist measured gives a way to quantify the chirality amplification [108, 109].

Another consequence of the unusually low  $K_{22}$  in LCLCs is that they are able to accommodate NPs [110] without much elastic energy penalty, by adopting a twisted deformation around the particles [111]. As discussed in Section 2.1 on chiral ligand-capped Au NPs in



thermotropic N-LCs, the efficiency of the transfer of chirality from chiral NP guests to the N-LC medium is significantly enhanced (by up to 50 times) if the molecules are attached to the surface of Au NPs or GNRs. Using the method described above for quantifying chirality amplification [108], a similar approach was pursued to explore if the same observation holds for LCLCs [109]. Here, the luminescent AMP-capped Au NCs were doped at 0.5 wt.% into DSCG/PEG (14.8 wt.%/0.8 wt.%), and the twist of the resultant tactoids compared to the case when neat AMP at the same low concentration was admixed into the same system [109]. The data showed that the AMP-Au NCs have  $\eta = 1.30^\circ \times 10^6 / (m \times \text{wt}\%)$  compared to  $\eta = 1.15^\circ \times 10^6 / (m \times \text{wt}\%)$  for AMP. To appreciate the impact of attaching the ligand to the surface of the Au NCs, note that the total molar concentration of AMP in AMP-Au NC sample is about a third of that in the neat AMP sample [109]. The nematic tactoids, therefore, provide a way to measure the chirality transfer from a weak inducer, for which other conventional POM methods (for instance the Grandjean-Cano method, or the fingerprint method) could not be used.

In the same study, a complementary technique, *i.e.* induced circular dichroism (iCD) spectrophotometry was employed to quantify the chirality transfer [109]. In this method, the sample is rotated at regular intervals and the CD spectrum is measured at each angle – the sum of the spectra is the iCD spectrum [109, 112]. The CD signal of interest is that of the helical supramolecular assembly the N\*-LCLC phase induced by the chiral NP additives [109, 112]. Other peaks in the CD spectrum could arise from absorption of the chiral ligands, electronic interactions of the ligands and the NPs, and from the plasmonic absorption of the NPs due to their periodic arrangement in the helical assembly (plasmonic CD bands) [109, 112].

Using this iCD method, a previous study already demonstrated the amplification of chirality by another bioorganic chiral molecule-capped Au NP, *i.e.* L-cysteine-capped Au NPs (L-cys Au NP), where the molar ellipticity of the induced N\*-LCLC phase was  $\sim$  four orders of magnitude greater for the L-cys Au NP doped sample compared to neat the one doped with L-cysteine itself ( $\Theta_{Lcys-AuNP} = 4.5 \times 10^{15} \text{ cm}^2 \text{ dmol}^{-1}$  vs.  $\Theta_{Lcys} = 1.5 \times 10^{11} \text{ cm}^2 \text{ dmol}^{-1}$ ) [112]. This is a remarkable increase in chirality transfer, considering that the number of L-cysteine molecules in the L-cys Au NP sample was as much as five orders of magnitudes lower than in the neat L-cysteine doped sample (Figure 14) [112].

To explain the higher efficiency of chirality transfer from the chiral Au NPs and NCs, the following model was proposed. The adsorption of chiral molecules onto the surface of the NPs and NCs localizes the chiral inducers, maximizing their chirality induction effect locally (acting

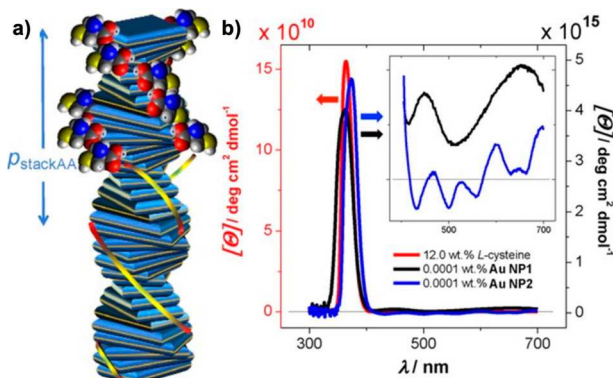


**Figure 14.** (a) Schematic of the arrangement of the DSCG molecules in an induced N\*-LCLC assembly and how the guest chiral molecules might be interacting with it. Shown in (b) are the iCD spectra of 12 wt.% DSCG in H<sub>2</sub>O doped with L-cysteine (red spectrum) or L-cysteine-capped AuNPs (black and blue spectra – Au NP1 and Au NP2, respectively, which are of slightly different average circle diameter). The inset in (b) shows the plasmonic CD peaks observed for the samples doped with the L-cys-AuNPs. Image is obtained with permission from reference [112] - Copyright 2017 WILEY-VCH Verlag GmbH & Co. KGaA, Weinheim.

as a network), which then translates to greater global chirality transfer [109, 112]. Also, fixing the ligand on to the plasmonic surface eliminates other interactions that may be extraneous to the chirality transfer. For instance, in the study comparing AMP-Au NCs to free AMP, at 7 wt.% AMP in DSCG, POM images show textures indicative of a columnar, M – phase or a coexistence between the N\* and M-phase (Figure 13a) [109]. For a comparable concentration of the AMP-Au NCs, evidence of an M-phase is not as obvious from POM images (Figure 13b). A possible explanation for this is that AMP intercalates into the DSCG assemblies or otherwise interacts with them, *e.g.* via hydrogen bonding, facilitating the formation of the M-phase [109]. When the ligand is affixed to the NC surface, however, its conformational freedom is somewhat limited. It is also likely that the chiral Au NPs or Au NCs coordinate to multiple DSCG assemblies, further enhancing the chirality transfer.

Even when they are hydrophilic and soluble in the isotropic liquid phase, NPs tend to have reduced solubility in N-LCLCs. This limits the concentration that can be doped into an LCLC before agglomeration to less than 1 wt.% [109, 110, 112]. The immiscibility of NPs in LCLCs is explained by the fact that the NPs introduce distortions to the alignment of the LCLC assemblies, resulting in an increase in the elastic free energy, which can be avoided by expelling the particles from the N-phase [110, 113]. This restriction to low NP concentrations poses a challenge in trying to quantify chirality induction by conventional POM techniques, where strong chirality induction would be required. The methods described above

overcome this problem. Using iCD makes it possible to quantify chirality transfer, while using tactoids enables the amplification of chirality of weak chiral inducers that could not be studied otherwise.

Though the studies surveyed in this section highlight the lack of insight into the precise mechanisms of chirality induction from nanomaterials in lyotropic LCs compared to their thermotropic counterparts, they also show their promise for several applications. Because lyotropic LCs are commonly aqueous systems, they are perfectly suited for applications in biosensing, among other technological applications. It is certain that more work still has to be done on understanding the interactions of chiral nanomaterials in lyotropic LCs, but the overall outlook is promising and exciting.

### 3. Chiral assembly of nanostructures

Nanostructure chiral assembly has been one of the most significant topics in the last decades combining nanomaterial chirality with the structural variety imparted by the various templating methodologies. [16, 114]. Here especially NP assemblies with helical topology are thought to provide access to unique applications in chiral plasmonics [115], biosensing [116], optomechanics [117], and metamaterials [118]. The quest for robust and efficient methods to precisely design chiral nanomaterial assemblies rapidly led to the use of LC phases and LC nanostructures as suitable templating motifs. In this section, we will begin with the chiral assembly of nanomaterials giving rise to CPL and then describe approaches to use B4-phase HNFs formed by select bent-core LCs [29].

#### 3.1. Chiral assembly using self-assembled organic as templates

##### 3.1.1. Strategies for circularly polarized luminescence (CPL)

CPL-active materials have attracted attention in particular in the fabrication of circularly polarized organic light-emitting diodes (CP-OLEDs) for numerous applications in 3D displays, optical data storage, and optical spintronic [119–123]. Compared to classical OLED displays where antireflective filters eliminate 50% of the nonpolarized light emitted from the pixel, CP-OLEDs exhibit high contrast and electroluminescence efficiency [124]. Enantioselective CPL sensors and probes for biological analytes and processes also emerged with the potential practical implementation of a CPL-based microscopy [125–129].

The degree of chirality in the CPL response is quantified by the luminescence dissymmetry factor [130],  $g_{lum}$ , that represents the difference emission intensity ( $\Delta I$ ) of left- ( $I_L$ ) and right-handed circularly polarized light ( $I_R$ )

divided by an averaged total luminescence intensity ( $I$ ) at a given frequency,  $\nu$ , by Eq. 3:

$$g_{lum} = \frac{\Delta I}{\frac{1}{2} I} = \frac{I_L - I_R}{\frac{1}{2} (I_L + I_R)} \quad (3)$$

Therefore, the highest absolute value of  $|g_{lum}|$  is 2 and corresponds to complete left- or right-handed circularly polarized emission.

Theoretically, the  $g_{lum}$  value is related to the photo-physical parameters of the chiral emitters:

$$g_{lum}(\lambda) = 4\text{Re} \left[ \frac{\mu^{gn} m^{gn}}{|\mu^{gn}|^2 + |m^{gn}|^2} \right] \quad (4)$$

where  $\mu^{gn}$  and  $m^{gn}$  refer to the electric and the magnetic transition dipole moments, respectively. Since the magnetic dipole transition moments are typically much smaller than the electric dipole terms, the denominator relates to the first term  $|\mu^{gn}|^2$ .

Eq. 4 indicates that a large  $g_{lum}$  factor can be reached in CPL-active materials when the transition considered is electric dipole forbidden, but magnetic dipole allowed. Chiral lanthanide(III) complexes possess intrashell parity-forbidden electric but allowed magnetic dipole transitions and generally show large dissymmetry factors between 0.1 and 1 [131]. For example, Eu(III) complexes have yielded up to 1.38 [132]. Nevertheless, the emission efficiencies of these complexes are typically small due to the nature of the involved metal-centred electronic transitions. In contrast, organic molecules exhibit higher emission yields and in addition present a wide-band emission that can be easily modulated as well as tuned. However, they usually display smaller  $g_{lum}$  factors typically within the range of  $10^{-3}$ – $10^{-2}$  due to the electric dipole-allowed transitions [133]. Hence, besides optimizing the molecular design of CPL-active materials [131, 133], it is crucial to develop new strategies to overcome their spectral instability and their emission efficiency to create high performance CPL systems. As polymers and supramolecules possess strong intramolecular and intermolecular interactions, optical activity within these architectures shows cooperative phenomena [134]. If the components are chiral, the transfer of their absolute configuration to the assembly leads to supramolecular chirality which constitutes an attractive way to provide CPL amplification [135, 136]. As such, studies on polymers and supramolecular structures are relevant to soft matter, as intramolecular and intermolecular chirality transfers can be induced in LCs. LCs can act as a host matrix for guest emitters. Thus, the long-range orientation of molecules in LCs has been utilized to fabricate helical stacks where the helical pitch can be temperature-dependent (in thermotropic liquid crystal) and the CPL

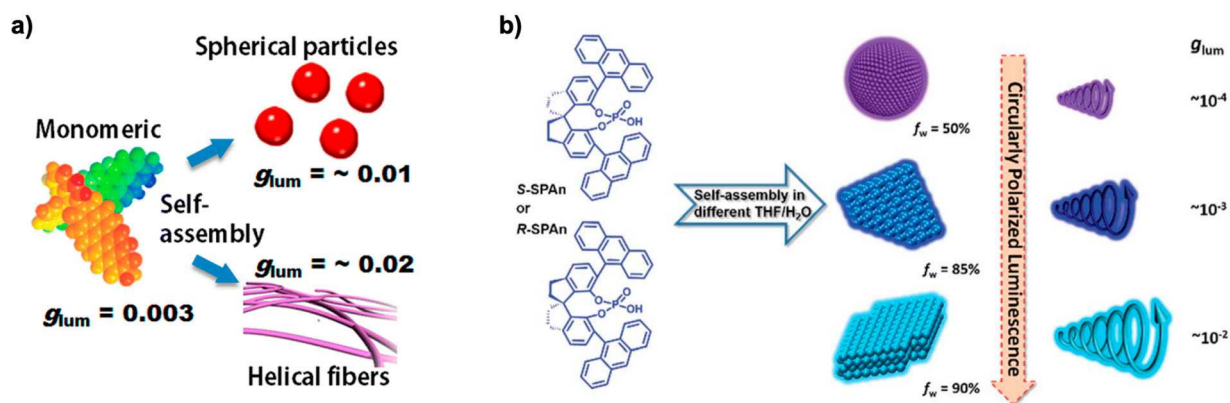


**Figure 15.** Examples of an assembly-enhanced CPL strategy showing the evolution of the dissymmetry factor with the self-assembly into different nanostructures using: (a) chiral perylene bisimide bichromophoric derivative possessing a 1,1'-binaphthalene bridge in mixed THF/H<sub>2</sub>O with different volume ratios. Reprinted with permission from [137] - Copyright © 2021, American Chemical Society. (b) Chiral emissive small molecules ((*R*)- or (*S*)-SPAN) in THF/H<sub>2</sub>O at different volume ratios. Reproduced with permission from reference [138] - Published by The Royal Society of Chemistry.

signal can be switched by an electric field generating the amplification of  $g_{lum}$  values, for example, through a phase transition of a thermotropic N\*-LC. Here, some examples of recent progress for the generation towards amplification of the CPL activity will be described. We focus on self-assembly approaches that serve to modulate the conformation as well as the spatial ordered arrangement of chiral emitters. Nevertheless, it has been proven that from solution to condensed phase the aggregation of chiral luminophores generally involves non-radiative pathways implying the quenching of the luminescence, called aggregation-caused quenching (ACQ) [133]. Therefore, beyond geometry, we also introduce some of the novel photophysical strategies that have been developed to manipulate and regulate the excited state of the chiral emitters and help build high dissymmetry factors. These recent advances have led to the production of CPL switching materials and the creation of CPL devices that will be considered at the end of this section.

As a first case, we analyse of the supramolecular self-assembly-enhanced CPL tactic applied by Kawai and co-workers to chiral perylenebisimide (PBI) systems in solution [137]. In the monomeric state of the molecule, a dissymmetry factor of  $10^{-3}$  has been observed. To stimulate high luminescence dissymmetry in the system, the excitonic coupling between PBI units observed in aggregated systems has been employed (Figure 15). The self-assembly of PBI into both spherical particles and helicoidal nanostructures enables the dissymmetry factor to be amplified and the  $g_{lum}$  values of a helical fibre assembly finally increased by one order of magnitude. This study as well as the recent work of Duan and co-workers on (11a*S*) and (11ab)-3,7-di-9-anthracenyl-10,11,12,13-tetrahydro-5-hydroxy-5-oxidediindeno[7,1*de*:10,70-*fg*]

[1,3,2] dioxaphosphocin ((*S*)-SPAN and (*R*)-SPAN) in assembled nanoparticles and 2D as well as 3D nanoflakes confirmed the multi-dimensional morphology control of the CPL (Figure 15b) [138]. These results demonstrate that regulation of the self-assembly, namely the molecular interactions within the assemblies, allows the modulation and the control of the chiroptical properties for the enhancement of the CPL.

Next, we will describe how the concept of aggregation-induced emission (AIE) associated with the geometry of the self-assembly can boost the chiroptical properties of a CPL-active material. In a condensed phase, the AIE mechanism takes advantage of a cooperative accumulation of dyes and counteracts the ACQ effect (Figure 16a). Indeed, in the aggregate state, the restriction of intramolecular motions enables generation of radiative decay and the molecule becomes a CPL-active material [139, 140]. Tang and team designed a propeller-shape  $\pi$ -conjugated molecule containing both an AIE-active silole core and chiral sugar pendants possessing extended electron delocalization involving the  $\pi$ -cloud [141]. This molecule shows no CD as well as no emission in solution but can assemble into hierarchical helical structures upon aggregation. Subsequently, chirality transfer occurs where the chiral sugar pendant together with the triazolylphenyl group induces the silole core to be helically arranged with a preferred screw sense. The CPL activity has been reported with two orders of magnitude increase in comparison with common organics material ( $g_{lum}$  values from  $-0.08$  to  $-0.13$  reported in Figure 16b). Beyond its geometry, the packing order of the assembly plays a critical role in CPL response. To reach an even higher  $g_{lum}$  value ( $-0.32$ ), the authors confined the helical pattern into a microchannel environment using a Teflon-based



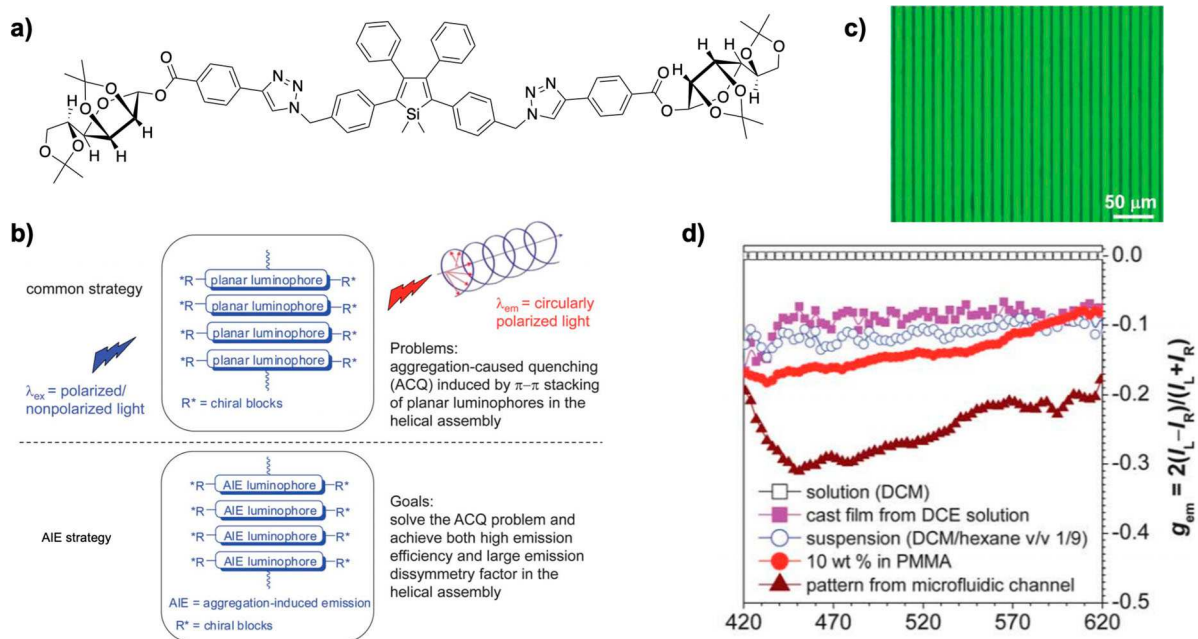


**Figure 16.** Example of assembly/aggregation-enhanced CPL: (a) Chemical structure of the mannose-modified silole AIE dye, (b) strategy to overcome the ACQ effect in conventional planar molecular design of luminescent chiral moiety (top), AIE luminophores strategy (bottom) allows accumulation of dyes in the self-assembled nanoscale matrices. (c) Fluorescence microscope images under UV excitation with the sample patterned in fabricated microfluidic channels and (d) plots of the CPL dissymmetry factor  $g_{lum}$  versus wavelength. The highest  $g_{lum}$  is observed under confinement of the helical pattern (wine-red curve; solid triangles corresponding to the sample show in (c)). Reproduced with permission from reference [141] - Published by The Royal Society of Chemistry.

microfluidic technique. More recently, a similar AIE strategy has been adopted by Deng *et al.* in chiral helical substituted polyacetylene supramolecular assemblies with nonetheless a specificity in the chirality transfer mechanism, the ‘matching rule’ between fluorescent moieties and chiral helical polyacetylene [142]. It consists of the overlap of the chiral component’s CD and the fluorescent component’s photoluminescence spectra without any type of covalent or noncovalent interactions specification needed between the two species.

Furthermore, materials that exhibit plasmon resonance enhancement have been exploited as novel CPL-active materials. Such materials exhibit electromagnetic field enhancement induced by localized surface plasmon resonance (LSPR) that can lead to plasmonic circular dichroism (PCD) as well as surface-enhanced fluorescence (SEF) [143]. Zhang and co-workers reported on achiral Eu-containing polyoxometalates  $\text{Na}_9\text{EuW}_{10}\text{O}_{36}$  ( $\text{EuW}_{10}$ ) that covered Ag NPs and electrostatically interacted with co-assembled chiral poly(ethylene oxide)<sub>114</sub>-*b*-poly(L-lysine)<sub>*n*</sub> ( $\text{PEO}_{114}$ -*b*-PLL<sub>*n*</sub>) to form coacervate core micelles with diameters of 50 nm (Figure 17) [144]. The Ag NPs,  $\text{EuW}_{10}$ , and PLL blocks of the polymer fashioned the core of the assemblies while the PEO blocks the outer shell. The CPL remained silent in the absence of the Ag NPs signifying non-effective dipole interaction between the chiral groups and the

emission species (Figure 17e) The CPL of  $\text{EuW}_{10}$  in Ag NPs/ $\text{PEO}_{114}$ -*b*-PLL<sub>109</sub>/ $\text{EuW}_{10}$  resulted from the surface-enhanced optical phenomena generated by the SPR effect of the Ag NPs near  $\text{EuW}_{10}$  which would significantly enhance the surrounding chiral electromagnetic field. Other photophysical strategies have been introduced in various self-assembled systems for energy and chirality transfers, such as Förster Resonance Energy Transfer [145] and Photon Upconversion based on Triplet–Triplet Annihilation [146]. For example, Liu *et al.* reported a chiral donor  $\pi$ -gelator that self-assembled into a helix with an achiral  $\pi$ -acceptor forming a composite donor–acceptor system in which the achiral acceptor generate both the supramolecular chirality and the circular polarized energy transfer from the chiral donor [145].

Doped chiral LCs have been widely used to achieve a high degree of CPL activity due to the unique optical property of reflection of circular polarized light. N\*-LCs allow to easily regulate the ordered arrangement of chiral emitters, to control the pitch of the assembly, and the stopband of the matrix. Furthermore, chiral LCs give access to chiroptical switches by using an external stimulus such as temperature, solvent, or an applied electric field for the dynamic modulation of CPL properties. Akagi *et al.* created a CPL-switchable cell containing the chiral disubstituted LC polyacetylene

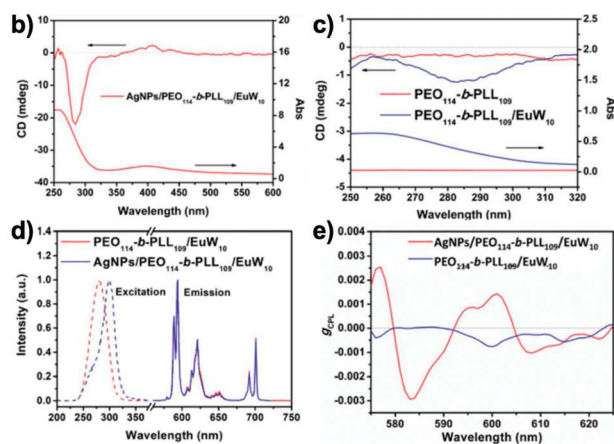
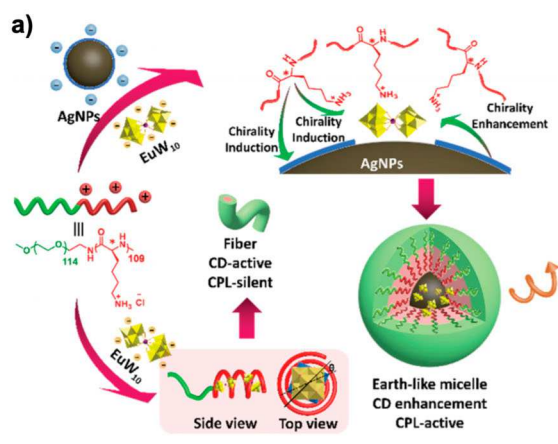


**Figure 17.** Example of plasmon-resonance-enhanced CPL in electrostatically co-assembled EuW10-containing supramolecular assemblies: (a) schematic illustration of the system based on an achiral EuW10 induced by the electrostatically co-assembled chiral (PEO114-*b*-PLL<sub>n</sub>) through long-term chiral transfer and improved by the surface plasmon resonance effect of Ag NPs. The CD and absorption spectra of (b) Ag NPs/PEO114-*b*-PLL109/EuW10, (c) PEO114-*b*-PLL109 and PEO114-*b*-PLL109/EuW10; (d) CPL spectra of Ag NPs/PEO114-*b*-PLL109/EuW10 and PEO114-*b*-PLL109/EuW10. Reproduced with permission from reference [144] - Published by The Royal Society of Chemistry.

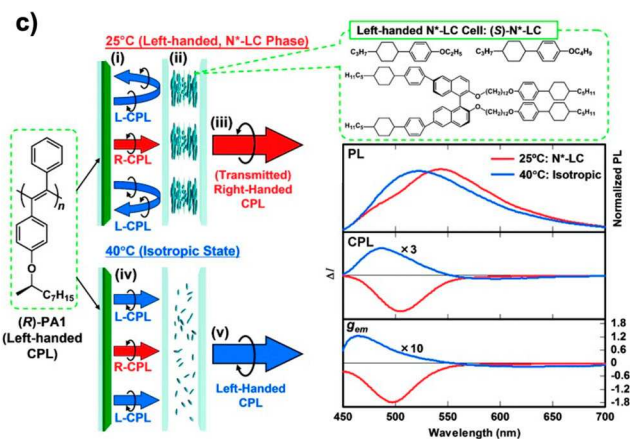
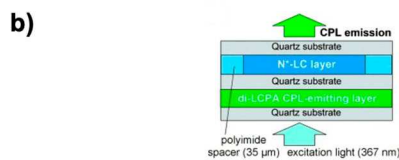
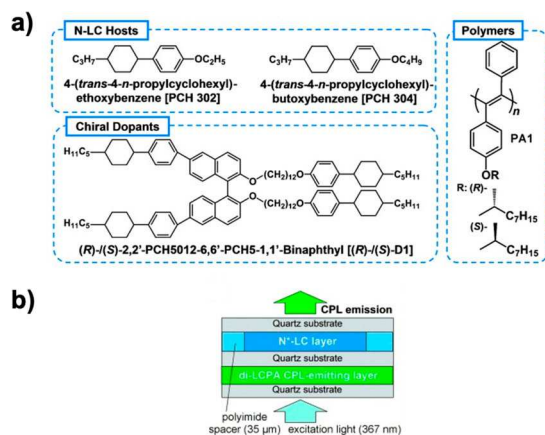


**Figure 18.** Example of liquid-crystal-enhanced CPL in: (a) chiral disubstituted LC polyacetylene (di-LCPA) film combined with a thermo-responsive  $N^*$ -LC using the nematic LC (N-LC) hosts PCH 302 and PCH 304, the chiral dopants (R)-D1 and (S)-D1, and the disubstituted LC polyacetylenes (R)-PA1 and (S)-PA1; (b) Schematic representation of the CPL-switchable cell; (c) Schematic representation of the first case discussed, namely (R)-PA1/(S)- $N^*$ -LC CPL-switchable cell, showing at room temperature: (i) the (R)-PA1 film emits predominantly left-handed CPL, (ii) the (S)- $N^*$ -LC cell selectively reflects left-handed CPL, and (iii) only right-handed CPL is transmitted and amplified; at 40 °C, (iv) no selective reflection of CPL; consequently, (v) predominantly left-handed CPL is transmitted. The PL, CPL, and  $g_{lum}$  (lower) spectra of the (R)-PA1/(S)- $N^*$ -LC CPL-switchable cell at 25 °C (red) and 40 °C (blue). Reproduced with permission from reference [147] - Copyright ©, Wiley-VCH.

(di-LCPA) film combined with a thermo-responsive  $N^*$ -LC (Figure 18) [147]. First, a CPL-switchable cell was prepared consisting of an (S)- $N^*$ -LC cell with an (R)-PA1 CPL-emitting layer (Figure 18b). The helical pitch of the  $N^*$ -LC layer was tuned and adjusted by addition of chiral dopant so that the selective reflection range was: (1) in the visible range and (2) coincided with the CPL wavelength of the di-LCPA film. The disubstituted LC polyacetylenes (R)-PA1 CPL-emitting film produced both left- and right-handed CPL with predominance of left-handed CPL (Figure 18c). The (S)- $N^*$ -LC cell enabled

the CPL to be dynamically switched through the phase change of the thermotropic  $N^*$ -LC cell and amplified from left- to right-handed CPL and *vice versa*. At room temperature, the (S)- $N^*$ -LC cell selectively reflected left-handed CPL and consequently only right-handed CPL was transmitted, leading to right-handed CPL amplification with a  $g_{lum}$  value of  $-1.79$ . In the isotropic liquid phase (at 40 °C), the helicoidal arrangement of the  $N^*$ -LC phase was absent and thus no selective reflection of left-handed CPL occurred. The predominantly left-handed CPL from the (R)-PA1 CPL-emitting layer was then

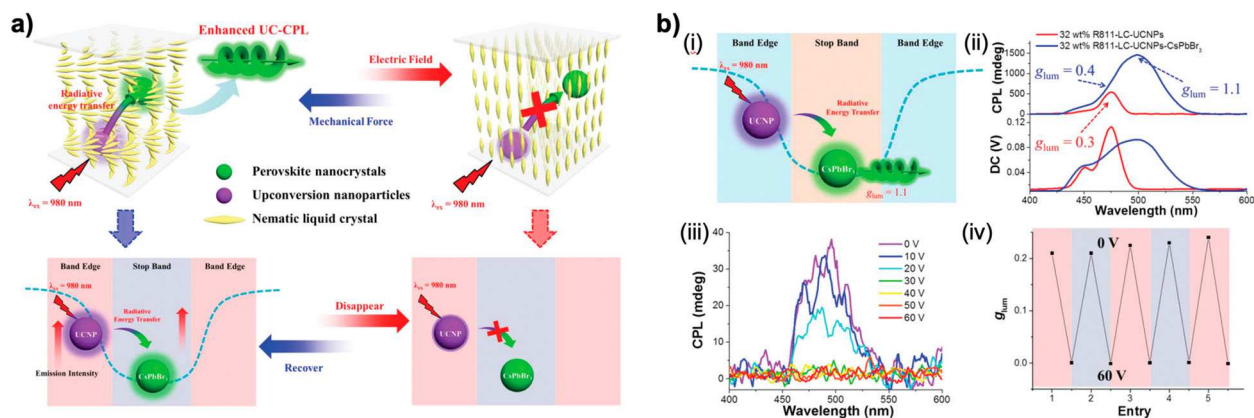


**Figure 19.** Example of photon upconversion-enhanced CPL in an LC matrix: (a) UC-CPL through the radiative energy transfer process from UCNPs (energy donor) to CsPbBr<sub>3</sub> PKNCs (energy acceptor). Their emission spectra were located at the edge and centre of photonic bandgap of N\*LC, respectively. The UC-CPL emission can be switched off by applying an electric field and recovered by applying a mechanical force. Thus, a voltage-force regulated switch of UC-CPL could be realized. (b) (i) Schematic representation of the radiative energy transfer process from UCNPs to CsPbBr<sub>3</sub> PKNCs in N\*LC; (ii) UC-CPL spectra of CsPbBr<sub>3</sub> PKNCs/UCNPs in N\*LC with different incident power of a 980 nm laser. The maximum value  $g_{lum}$  of CsPbBr<sub>3</sub> PKNCs was 1.1. The UCNPs showed similar UC-CPL signals at 475 nm with or without CsPbBr<sub>3</sub> PKNCs, whose  $g_{lum}$  value was 0.4 and 0.3, respectively; (iii) UC-CPL spectra of CsPbBr<sub>3</sub> PKNCs under the different voltages; (iv) intensity of the UC-CPL  $g_{lum}$  value of the CsPbBr<sub>3</sub> PKNCs against the repeated voltage-force exposure cycles. Reproduced with permission from reference [149] - Copyright ©, Wiley-VCH.

transmitted with a  $g_{lum}$  value of +0.125. Similarly, a CPL-switchable cell with opposite handedness (R)-N\*LC was also prepared with an (S)-PA1 CPL-emitting layer showing  $g_{lum}$  values of respectively +1.77 at room temperature and -0.146 in the isotropic liquid state.

Likewise, these LC materials can be controlled externally using electric fields, allowing the manipulation of polarization properties *in situ*. Morris *et al.* presented an electrically switchable CPL device using transition metal clustomesogen luminophores dispersed in an N\*LC matrix [148]. These emitters known to combine the specific properties of nanoclusters (magnetic, electronic, luminescence) with the anisotropy-related properties of LCs present the advantages of being photostable, exhibiting high quantum yields (up to 1), and an ability to be dispersed at high concentrations into LC materials. The investigated mixture consisted of a [Mo<sub>6</sub>I<sub>8</sub>(OCOC<sub>2</sub>F<sub>5</sub>)<sub>6</sub>] cluster-based clustomesogen with a tris(w-[4-(4'-cyanobiphenyl)oxy]decyl)methylammonium cation (Trisel<sub>2</sub>[Mo<sub>6</sub>I<sub>8</sub>(OCOC<sub>2</sub>F<sub>5</sub>)<sub>6</sub>]), the achiral nematic LC ZLI-1840, and the chiral additive BDH1281. As in previously reported studies, the N\*LC photonic band gap overlapped with the clustomesogen phosphorescence (with 2.2 wt.% BDH1281 and 20 wt.% clustomesogen in ZLI-1840), resulting in strong CP emission with a dissymmetry factor of 1.6. Under an applied external electric field ( $E = 1.3 \text{ V } \mu\text{m}^{-1}$ ), the N-LC homeotropic alignment, the helicoidal structure was lost and  $g_{lum}$  reached 0, enabling the switch-off of the structure. Recently, Duan and co-workers tested a similar approach by incorporating upconversion nanoparticles

(UCNPs) and CsPbBr<sub>3</sub> perovskite nanocrystals (PKNCs) into an N\*LC (Figure 19) [149]. The UC-CPL phenomenon induced in the achiral CsPbBr<sub>3</sub> PKNCs derived from the radiative energy transfer process from UCNPs (energy donor) to CsPbBr<sub>3</sub> PKNCs (energy acceptor). By locating the emission peaks of CsPbBr<sub>3</sub> PKNCs and UCNPs at the centre and edge of the photonic bandgap of the N\*LC respectively, the maximum  $g_{lum}$  value of UC-CPL can be amplified to a large value of 1.1. Additionally, the enhanced emission of UCNPs could be reabsorbed by the CsPbBr<sub>3</sub> PKNCs, further enhancing the emission of CsPbBr<sub>3</sub> PKNCs. This UC emission and the radiative energy transfer can be electric field controlled.

By the further addition of a chiral fluorescent dopant capable of photoswitching as well as photodissociation to an N-LC already doped with UCNPs, Juan and co-workers were able to demonstrate an upconversion-luminescence-induced nanocomposite photoswitch that could additionally be patterned [150].

Finally, we will consider how multidomain cholesteric emitting layers can combine semiconducting and photonic functionalities to make OLEDs emitting CP electroluminescence (CPE). OLEDs can emit circularly polarized electroluminescence (CPEL) when the emitting organic material is chiral and of one handedness only. Friend and team exploited a chiral and enantiomerically pure substituted polyfluorene copolymer poly(fluorene-alt-benzothiadiazole) (c-PFBT) used as emitting layer in the OLEDs (Figure 20) [151]. The polymer contained a fluorene-benzothiadiazole



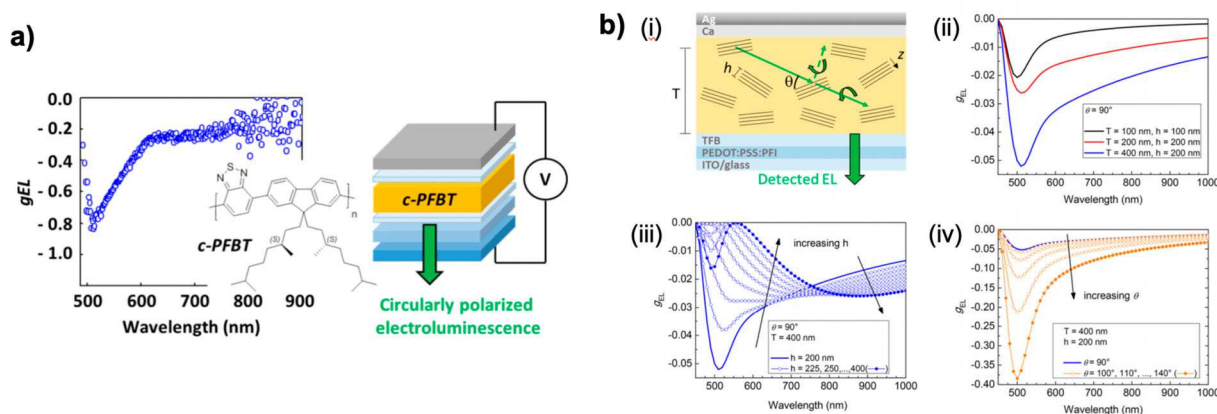


**Figure 20.** Schematic representation of: (a) the CP-OLED developed by Friend *et al.* [151] consisting of the hole injection layer (PEDOT:PSS:PFI) deposited on top of ITO, the emitting layer (c-PFBT) and the electron injection layers (calcium and silver).  $g_{EL}$  of  $-0.8$  was reached under pulsed voltage; (b) (i) the polycrystalline  $N^*$ -LC film in the OLED stack. The  $N^*$ -LC domains are represented by groups of black lines ( $z$  being the direction of the cholesteric helical axis). The direction of detection of electroluminescence (EL) with respect to the substrate is also shown; (ii) calculated  $g_{EL}$  for different values of  $T$  and  $h$ ; (iii) and (iv) evolution of  $g_{EL}$  with the parameters  $h$  and  $\theta$ , respectively, for  $T = 400$  nm. Reproduced with permission from reference [151] - Published by the American Chemical Society.

donor-acceptor repeat unit forming the conjugated backbone, with chiral centres attached to the fluorene moiety. Thermal annealing led to the self-assembly of the polymer into a multidomain  $N^*$ -LC film. CPEL with up to 40% excess of right-handed polarization was reached under pulsed voltage bias operation ( $g_{EL} = -0.8$ ) and 30% ( $g_{EL} = -0.6$ ) under constant voltage bias. CPEL originated from circular selective scattering and birefringence in such multidomain films (Figure 20b).

In this subsection, we have shown that the CPL-activity can be built, manipulated, and controlled using specific strategies based on photophysical regulation of the excited state of the chiral emitters as well as their conformation and spatial ordered arrangement. The amplification of the CPL-response in active LC-based material paves the way for the design of efficient CPL devices for a wide range of technologically oriented applications. However, aside from the  $N^*$ -LC matrices, other LC phases are suitable for the helical assembly of nanostructures as well, and emissive NP-LC mixtures will continue to be an active segment of research considering a wealth of opportunities for optical and photonic applications [152].

### 3.1.2. Chiral organic nanostructures – helical nano- and microfilaments

One such highly interesting phase formed by bent-core liquid crystal molecules is the B4-phase, frequently also referred to as the helical nanofilaments phase [29], in which twisted bundles of smectic layers form, chirality preserving [153] with self-limiting width but not in the length [154]. HNFs are characterized by a constant width of  $\sim 40$  nm and a helical pitch of  $\sim 200$  nm [29].

The width and the pitch, *i.e.* the morphology, depend on the chemical structure, and recent work has shown that by strategically introducing chiral centres into the side chains they can form helical microfilaments [155], helical-layered nanocylinders [156], a variety of dual modulated HNFs [157–159], and even twisted or flat nanoribbons (Figure 21) [160]. These morphologies are considered to be semi-crystalline [161], *i.e.* hence robust, which makes them most suitable as templates for the non-solvated assembly of plasmonic and other nanomaterials. The orientation of these nano- or micrometre-scale twisted bundles can be controlled in various ways including conventional treatment methods such as the rubbed polymer alignment using a nematic LC [162, 163], photoalignment [164], microchannels [165], and cylindrical nanoconfinement [166]. The control of each alignment and nanometre helical twist has already led to studies seeking applications such as chiral sensing of optical activity [167], and use as templates for nanomaterial assemblies as outlined here.

Lewandowski and co-workers used this inherently robust HNF template to helically assemble Au NPs and GNRs (Figure 22a) [168]. While HNFs tend to expel guest molecules [169, 170], recent research also showed that admixing (pro)mesogenic molecules can alter the B4 morphology [171–173]. However, by decorating plasmonic nanomaterials (polyhedra and rods) with a structurally closely related ligands, thereby enhancing the compatibility between the nanomaterial additive and HNF host, previously used to achieve magnetically reconfigurable nematic-like [174] or columnar assembly of GNRs [175], the group was able to assemble both Au NPs and GNRs in a double-helical fashion at the two sides

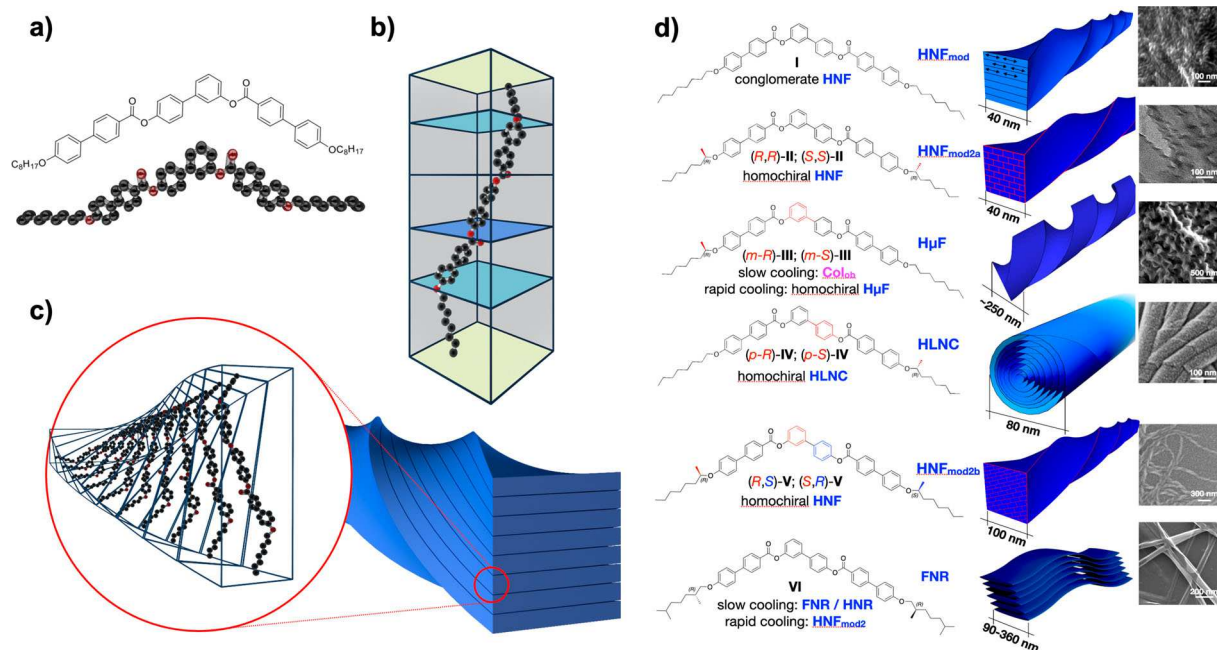


**Figure 21.** B4 morphologies: (a) chemical structure and basic model of a tris-biphenyl diester bent-core LC molecule, (b) illustration of such bent-core molecule in smectic sublayers, where orthogonal packing reference of top and bottom molecular halves leads to frustration that is relieved by local saddle splay leading to the assembly and limited growth of bundles of smectic layers as show in (c) for helical nanofilaments (HNF morphology). (d) Depiction of the different B4-phase morphologies (with representative electron microscopy images) formed by tris-biphenyl diesters with strategically introduced chiral centres in the aliphatic side chains: I [158], II [158], III [155], IV [156], V [159], and VI [160].

of layer edges of the HNF facilitated by core-core interactions between HNF host and structurally related ligand molecules. Furthermore, using an approach dubbed chirality synchronization, these co-assemblies of HNFs and plasmonic nanomaterials were interrogated by micro-CD experiments (Figure 22b) [176]. A related approach, leading to a helical assembly of GNRs, used human islet amyloid polypeptides (hIAPPs) and a transition from randomly coiled hIAPPs into twisted fibrils with  $\beta$ -sheet structures [177].

HNFs, however, can also be utilized as inverse templates [178]. Bent-core molecules thoroughly mixed with rod-like, photopolymerizable N-LC monomers initially form the expected nano-segregated mixture following the earlier-mentioned concept of HNFs expelling guest molecules. After UV-irradiation (*i.e.* polymerization) and washing out the bent-core HNF host, the resulting polymer network now mimics the nanoporous structure of the washed out HNFs, which is then back-filled with an achiral N-LC (here 5CB). CD data taken along the entire process demonstrate that the nanoporous inverse HNF template can memorized and efficiently transfer chirality (Figure 23). The induced chirality (racemic overall but opposite in adjacent domains, which is due to the chiral conglomerate of HNFs formed by the achiral bent-core molecules) can further be controlled (or turned On

and OFF) by changes in temperature (*i.e.* going through the phase transition to the isotropic liquid phase) and an applied electric field. This approach in combination with the afore-mentioned concepts of CPL and AIE is certainly feasible if emissive nanomaterials or appropriate fluorescent dyes are introduced into these inverse templates.

Related and highly fascinating structures can also be realized by Au nanoplates (with an average size of 5 nm) functionalized with L-, D- or DL-cysteine [179]. Cations adsorbed on the surface of these Au nanoplates cause increased electrostatic repulsion, which prevents stochastic agglomeration when the repulsion is sufficiently, leading to hierarchical organized particle assemblies with twisted nanoribbon shapes, self-limiting in lateral dimensions, as reviewed recently by Grason [154], when nonracemic L- and D-cysteine ligands are used, and non-twisted with racemic DL-cysteine (Figure 24) [178]. Similar self-limiting and self-assembled supraparticles were previously reported by Glotzer and Kotov *et al.* using citrate-capped semiconductor NPs [180].

With increasing zeta potential,  $\zeta$ , achieved by the addition of surfactant cations, *i.e.* cetyltrimethylammonium (CTA<sup>+</sup>), these Au nanoplates tended to assemble edge-to-edge rather than face-to-face forming the afore-mentioned twisted nanoribbon, which closely

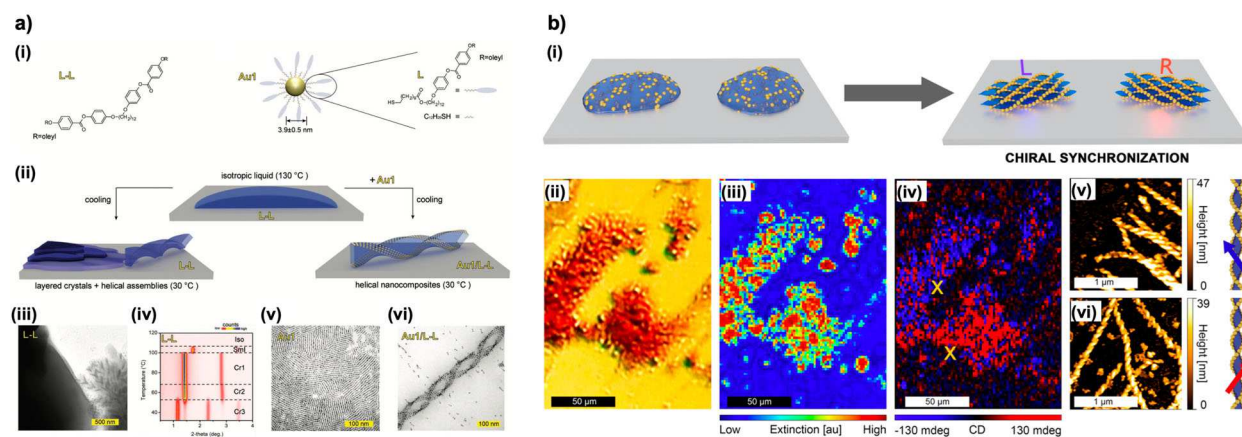


**Figure 22.** (a) Double-helical assembly of Au NPs and GNRs: (i) Chemical structure of bent-shaped LC (L-L) and L-ligand-capped Au NPs (Au1), (ii) illustration of morphologies formed by neat L-L and by the mixture of L-L and Au1 on cooling from the isotropic liquid phase, (iii) TEM image of pure L-L shows layered crystalline and HNF structures, (iv) XRD data of L-L depending on the temperature, and (v and vi) TEM images of (v) Au1 and (vi) the mixture of L-L and Au1 showing the double-helical assembly of the Au NPs. Reproduced with permission from reference [168] - Copyright ©, Wiley-VCH. (b) Chiral synchronization and micro-CD: (i) graphical depiction of the approach, (ii) optical micrograph, (iii) extinction intensity map at 550 nm, (iv) CD microscopic mapping at 550 nm, revealing the presence of either handedness, and (v and vi) corresponding AFM images. Reproduced with permission from reference [176] - Published by the American Chemical Society.

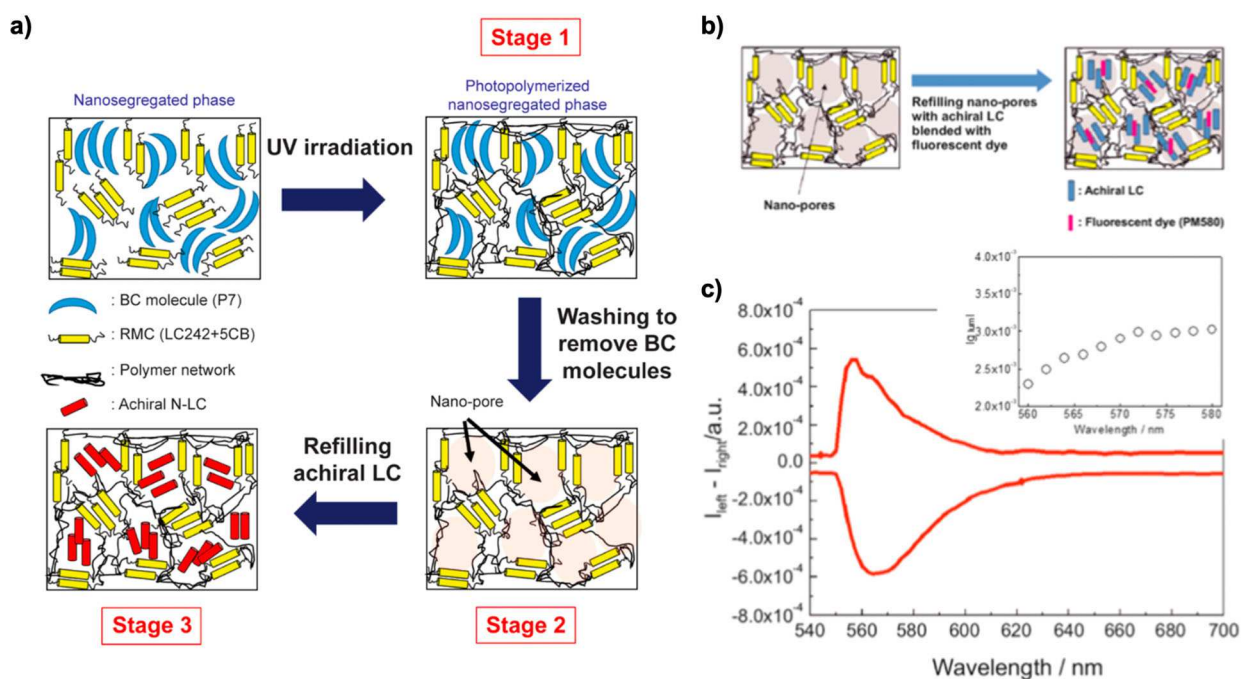


**Figure 23.** (a) Sketch of templated three-stage formation of an inverse chiral HNF network, (b) refilled chiral network using an achiral N-LC as well as a fluorescent dye, and (c) CPL spectra of the composites for chiral domains with opposite handedness (HNF conglomerate) at room temperature; overlay shows the plot of  $|g_{lum}|$  vs. wavelength maxing out at  $\sim 3 \cdot 10^{-3}$  at around 580 nm. Reproduced with permission from reference [177] - Published by the American Chemical Society.

resemble the twisted smectic layers of B4-phase HNFs. These nanoribbons ultimately assemble as spikes radially around an axis according to their ligand configuration (D- or L-cysteine), giving rise to micron-scale coccolith-like supraparticles with distinctive CD spectra. However, flat kayak-shaped supraparticles with a

layered architecture were observed when the nanoplates were capped with racemic DL-cysteine at the Au nanoplate surface [178], in analogy to the FNRs formed by some of the afore-listed bent-core molecules with diminished chirality such as compound VI [160] in Figure 21d.



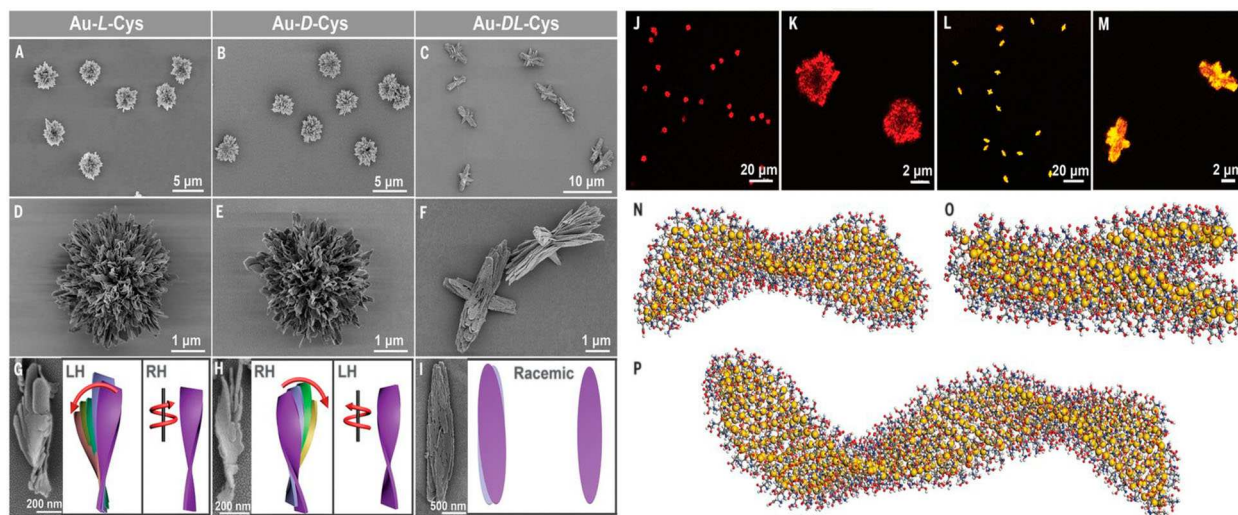


**Figure 24.** (A - F) SEM images of Au-L-Cys, Au-D-Cys, and Au-DL-Cys coccolith- and kayak-like particles. (G - I) SEM images and schematic drawings of twisted (G and H) and flat nanoribbons (I) forming the supraparticles shown in (A - F). (J - M) Confocal microscopy images of coccolith- and kayak-like supraparticles, and (N - O) atomistic MD simulation of twisted conformation of Au-L-Cys single sheets of different length (N and P) and their stacks (O). Reproduced with permission from reference [178] - Reprinted with permission from AAAS.

Similar effects on shape selection for supramolecular architectures with increasing or decreasing chirality, have also been reported for other, structurally diverse systems such as Gemini surfactants [181] or bile acid end-modified *p*-phenylene ethynylene oligomers [182] among others [183], thereby underlining the general applicability of chirality, or better, enantiomeric enrichment controlled self-assembly into supramolecular and supraparticulate architectures.

### 3.2. Chiral assemblies of DNA nanostructures

In this section we will focus on the formation of lyotropic  $N^*$ -LC phases that occur in DNA supramolecular assemblies. Double stranded (ds) DNA adopts a right-handed double helix (B-form DNA). This is the common form of DNA that exists under normal physiological conditions, and in the context of the origins of life, the spontaneous LC self-assembly of DNA has been proposed as a route in the evolution of primordial nucleic acids [184]. Thus, the molecular ordering within LC domains in which the ends of particular oligomers are held in close vicinity by packing and stacking forces, could have operated as a template for the formation and ligation of extended DNA chains under favourable chemical conditions [185]. This potential relevance, motivated Bellini *et al.* to investigate the formation of  $N^*$ -LC phases by ultra-short double helix oligonucleotides (nDNA) dispersed at high concentrations in water (Figure 25) [186], which contradicted Onsager theory [187]. Different sets of single stranded (ss) DNA sequences exhibiting several lengths, abilities to engage in end-to-end aggregation,

and with mutual or self-complementarity, were used. Interestingly, small changes in oligomer length/sequence, or alterations in the mode of end-to-end aggregation, significantly affected the hierarchical supramolecular LC order of nDNA, *i.e.* right-handed phases were only found for oligomers shorter than 14 base pairs (bp), and for DNA sequences that exhibited transitions to the  $N^*$ -LC phase at concentrations higher than  $620 \text{ mg mL}^{-1}$ ;  $N^*$ -LC handedness inversion from left- to right-handed occurred at higher concentrations of nDNA, and the observed  $p$  matched the  $p$  of ds B-DNA; shorter oligomers tended to show shorter  $N^*$ -LC  $p$  values well within the visible range, while sequences with more than 12 bp showed  $p$  values of  $1 \text{ }\mu\text{m}$  or higher.

The same group, proceeded to investigate the minimal oligomer length required for DNA  $N^*$ -LC formation [188]. Thus, an extremely short DNA sequence containing only four-base-long oligomers (5'-GCTA-3') was designed to simultaneously interact by Watson-Crick base pairing on either the 5'-end, GC/CG, or the 3'-end, TA/AT. The aggregates originated by base pairing, led to the formation of oligomers assembled in running-bond type chains of multiple DNA strands. In addition to Watson-Crick base pairing, coaxial stacking, which is the stacking interaction between the terminal bases of two nicked strands, and dangling ends stacking, *i.e.* the stacking of the first unpaired nucleobase in the overhang with the adjacent paired ones, were proposed as interactions that contributed for the stability of the formed double helix. Moreover, thermal stability of the assembled DNA duplexes  $N^*$ -LC phase increased with DNA concentration, as expected for lyotropic LCs. In addition, the twist

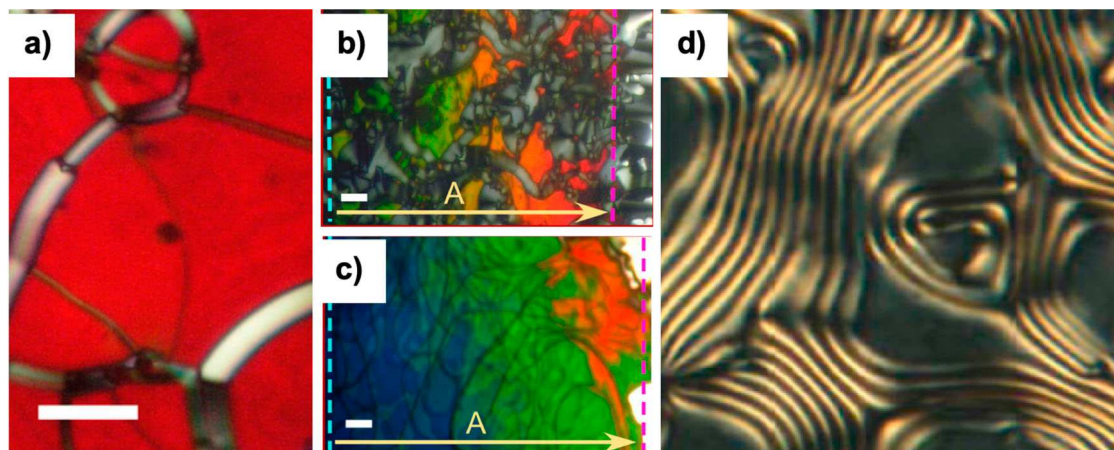


**Figure 25.** Examples of  $N^*$ -LC textures of ds nDNA, observed between crossed polarizers: (a) oily streaks texture. (b and c) Dependence of the  $N^*$ -LC pitch on the concentration in cells with a concentration gradient: (b) under left-handed helix forming conditions and (c) under right-handed inducing conditions. (d) Fingerprint texture. Scale bars in all images: 30  $\mu\text{m}$ . Reproduced with permission from reference [185] - Copyright © 2010 National Academy of Sciences.

of the nematic director was found to be left-handed, with  $p$  at values in the visible spectral range. Interestingly, an increase of temperature caused  $p$  to decrease, which was reflected in a significant colour change in the selective reflection wavelength, as seen in Figure 26.

Fraccia and co-workers have also investigated the LC behaviour of short DNA oligomers, and focused their studies on blunt-ended 12bp dsDNA oligomers derived from the Dickerson Dodecamer [189]. These oligomers had three different types of 5'-termini chemistry: 5'-OH,

5'-phosphate (P), and 5'-PPP [190], which were conceived for the discernment of the way different P termini disturb the stacking of DNA duplexes. Surprisingly, all three types of dsDNA oligomers were able to form  $N^*$ -LC phases (Figure 27), and the one with 5'-PPP termini could also form columnar textures.

In addition, it was observed that  $p$  of the  $N^*$ -LC phases was on the micrometre range and slightly increasing with temperature. Moreover, the  $N^*$ -LC phases showed left-handedness as a result of the combination of the steric

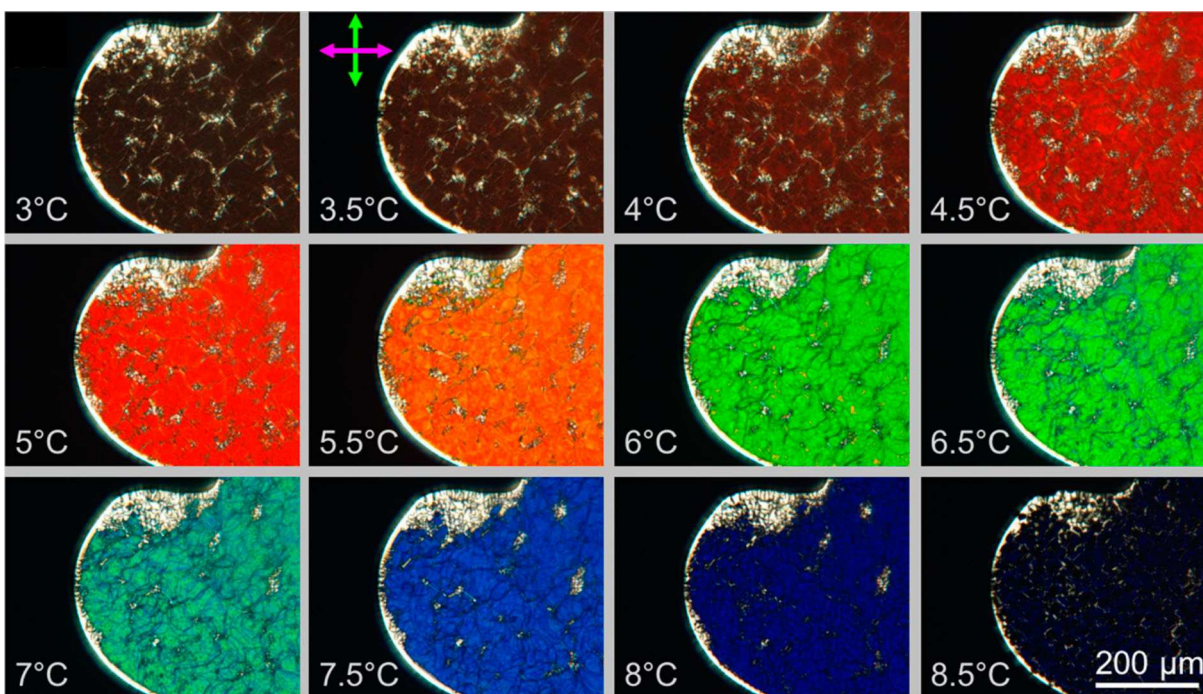


**Figure 26.** Photomicrographs depicting a  $N^*$ -LC domain with increasing temperature; changes in colour are due to alterations of the selective reflection wavelength, which correlates to variations of  $p$ . Reproduced with permission from reference [187] - MDPI.



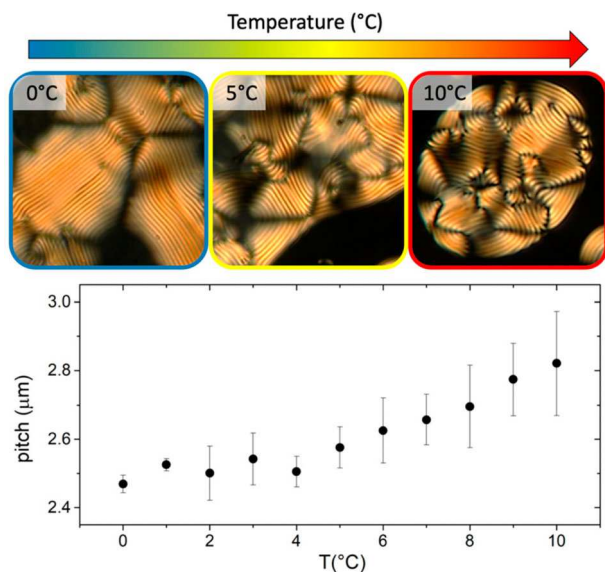


**Figure 27.** Photomicrographs of the fingerprint textures formed by 5'-PPP dsDNA oligomers, where  $p$  increases with increasing temperature. Reproduced with permission from reference [189] - Published by Taylor & Francis.

interactions between dsDNA oligomers, which favour the propagation of the right-handedness of the DNA helix, and the electrostatic repulsion, which instead favours left-handed chirality. The occurrence of the LC phases in the 5'-PPP dsDNA oligomers indicates that attractive stacking interactions still prevail and are able to induce linear aggregation.

The formation of LC coacervates in systems composed of short dsDNA of 12bp and poly-L-lysine (PLL), was investigated by Fraccia and Jia. In this system, four different types of LC phases were reported: isotropic,  $N^*$ , axial columnar and high order columnar [191]. LC self-assembly was proposed to be due to the reversible linear aggregation of dsDNA into supramolecular structures within the dense coacervate phase, and all LC phases could be accessed with continuity through different concentrations of DNA and PLL as well as variations in ionic strength and temperature. Moreover, the  $N^*$ -LC phase exhibited right-handed chirality, with  $p$  longer than  $5 \mu\text{m}$  within the LC-coacervate droplets (Figure 28). The right-handed chirality was due to the high salt concentrations,  $[\text{NaCl}] = 800 \text{ mM}$ , which allowed steric side-side interactions between dsDNA. In addition, the LC-coacervate phases retained fluidity, and their assembly was proven to be dynamic and reversible.

Another interesting example arises from the DNA nanotechnology field, which uses the programmability of DNA for the construction of very precise supramolecular DNA nanoarchitectures of arbitrary structural complexity, such as DNA origami [192–194]. Dogič *et al.* have recently shown that monodispersed DNA origami-based architectures that mimicked the geometry of filamentous phages, formed a  $N^*$ -LC phase at concentrations above  $37 \text{ mg mL}^{-1}$  [195]. The filamentous phages DNA origami analogues were prepared in four variants exhibiting different degrees of twist along the filament's axis, and consisted of 6-helix origami filaments with a diameter of

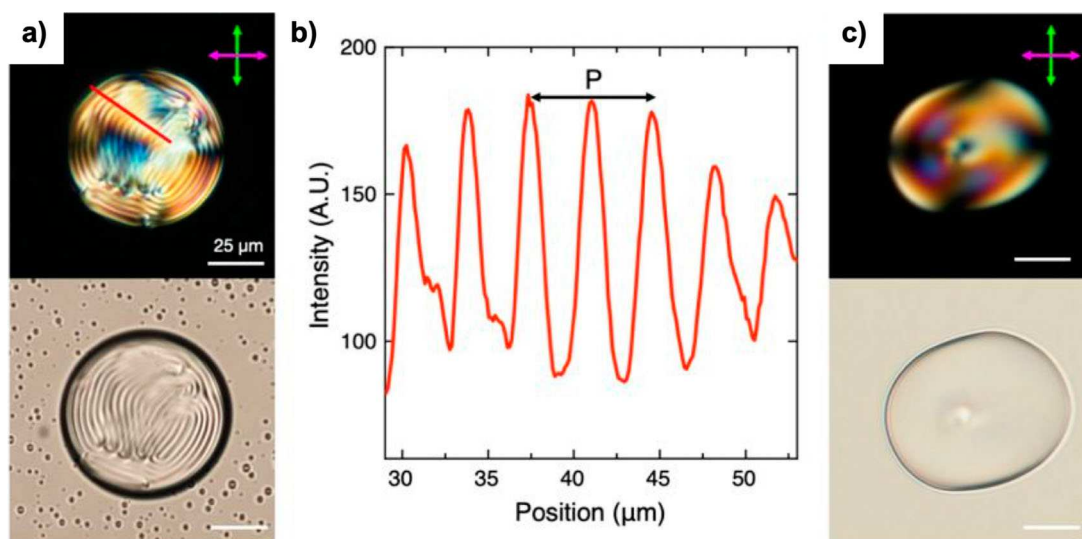


**Figure 28.** Characterization of the cholesteric  $p$  in short 12bp dsDNA LC-coacervate droplets: (a) fingerprint texture, top polarized optical microscopy (crossed polarizers), and bottom bright field microscopy. (b) Intensity profile measured on the red line, which crosses the  $N^*$ -LC droplet in (a) allows the measurement of  $p = 7.4 \pm 0.5 \mu\text{m}$ . (c)  $N^*$ -LC phase of a droplet from an aged sample that shows a  $p$  that exceeds the micrometre range; scale bars:  $25 \mu\text{m}$ . Reproduced with permission from reference [190] - Published by the American Chemical Society.



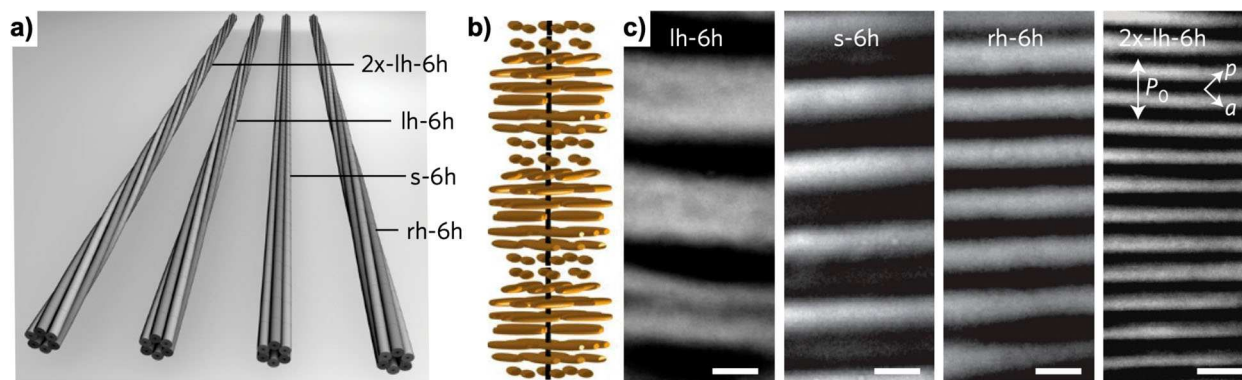


**Figure 29.** DNA origami-based  $N^*$ -LCs. (a) Structure of different DNA origami filaments with varying twists along the filament's long axis that were used for the assembly of bulk LC phases. The filaments consisted of 2x-left-handed six-helix (2x-lh-6h), left-handed (lh-6h), straight (s-6h), and right-handed (rh-6h) filaments. (b) Schematic representation of the  $N^*$ -LC helix. (c) Polarized optical photomicrograph of the samples. The concentration of all  $N^*$ -LC samples is  $37 \text{ mg mL}^{-1}$ , and the ionic strength is  $260 \text{ mM}$ . Dark lines represent the regions where the rods are perpendicular to the image, and the bright lines correspond to regions where rods are in the image plane; scale bars:  $20 \mu\text{m}$ . Reprinted with permission from reference [194] – Published by Nature/Springer/Palgrave, Copyright © 2017.

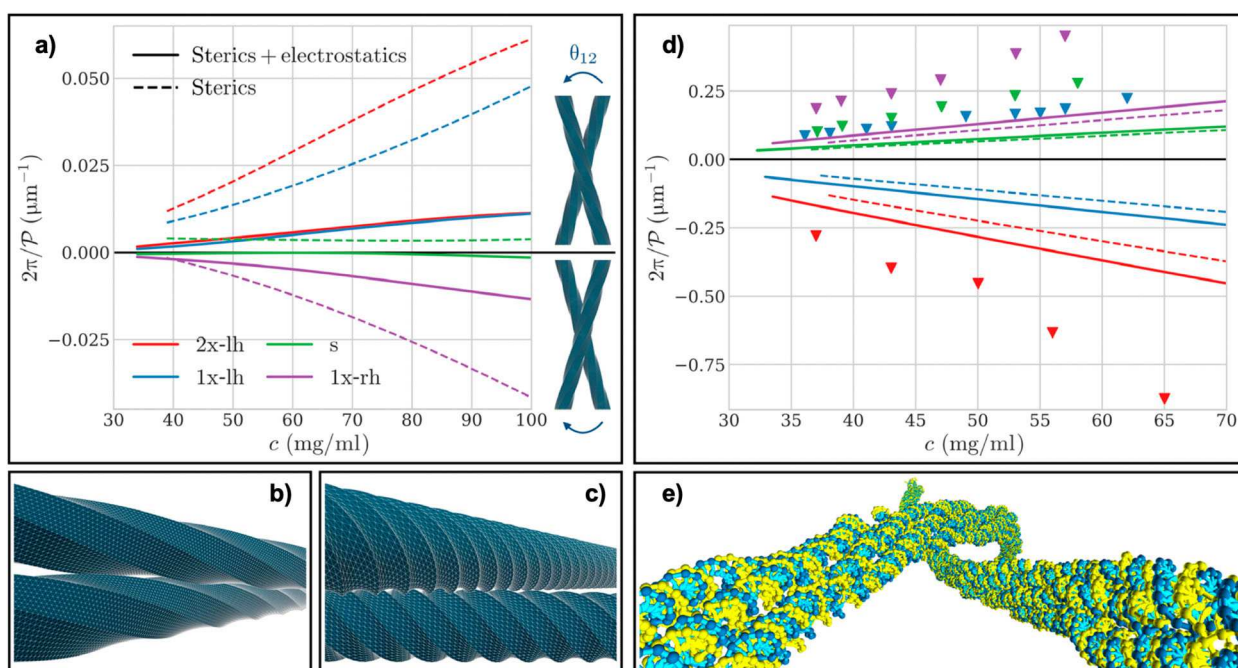


**Figure 30.** Cholesteric assembly of ground-state and thermalized DNA origamis: (a) inverse equilibrium of pitch as a function of particle concentration for ground-state filament conformations. Dashed lines denote values obtained by assuming pure steric interactions and solid lines by accounting for both steric and Debye-Hückel repulsion. Positive (resp. negative) values of  $p$  correspond to lyotropic  $N^*$ -LC phases bearing right (resp. left) handedness, as illustrated at right. (b) Close-approach configuration of idealized, weakly twisted right-handed filaments displaying a left-handed arrangement. (c) Same as (b) for the case of strongly twisted right-handed filaments, illustrating their entropic preferences for right-handed arrangements. (d) Same as (a) for the case of thermalized filaments. Markers denote experimental measurements (*i.e.* from [194]). (e) Angular configuration minimizing the chiral two-body potential of mean force for thermalized 1x-lh origamis, illustrating the predominance of long-wavelength backbone fluctuations over local axial twist in their lyotropic  $N^*$ -LC assembly. Reproduced with permission from reference [195] – Copyright © AAAS.

9, 420 nm contour length,  $2.4 \mu\text{m}$  persistence length, and polydispersity below 3% (Figure 29a).

It was observed that the twist inscribed along the origami filament's long axis exerted great influence on  $p$  of the bulk cholesteric phases, *i.e.* straight 6-helix DNA origami filaments formed a right-handed  $N^*$ -LC phase,

while filaments with a  $360^\circ$  inscribed right-handed twist showed smaller values of  $p$ . Contrary, filaments with  $360^\circ$  of left-handed twist produced larger  $p$  (Figures 29b and c). Interestingly, filaments with a further increased left-handed twist yielded a very tightly twisted  $N^*$ -LC phase.

On a theoretical note, Doye and co-workers adopted similar DNA origami models to the ones presented by Dogič *et al.* to provide theoretical evidence of the mechanism of chirality amplification of rod-shaped soft matter in lyotropic N<sup>\*</sup>-LCs (Figure 30) [196].

Their calculations indicated that phase chirality in those systems arises from weak fluctuation-stabilized solenoidal writhing of the DNA origami backbones, and thus largely dictated by intramolecular mechanics. Moreover, the net helicity of the backbone fluctuations was found to originate from the weak over- or underwinding of the constituent DNA double strands in the origami ground states. Thus, subtle long-ranged conformational features were proposed to govern macroscopic chiral organization, rather than local chemical structure.

Finally, it is important to highlight that DNA-origami nanostructures have been extensively used for the chiral and helical assembly of plasmonic and semiconductor nanomaterials [193, 197–203], though much less frequently in combination with liquid crystalline DNA nanostructures [204]. Considering the aforementioned strategies of tuneable pitch and handedness, this research domain will surely see more emphasis in the near future [205].

#### 4. Summary and outlook

The combination of nanomaterials and liquid crystals to better understand chirality transfer across length scales and assemble nanomaterials in chiral (helical) fashion has seen significant advances over the past several years. Liquid crystal phases should see a growing use as an experimental measure for chirality transfer efficiency, supporting data from spectroscopic and geometrical approaches to quantify chirality itself, since the ability of a material to transfer chirality to its surrounding medium is a significantly more critical measure for most applications of chiral nanomaterials in sensing [206], optics [207], and photonics [208]. Thus far, most experimental systems relied on the induced N<sup>\*</sup> and SmC<sup>\*</sup> phase [41, 44, 50, 209], but other chiral LC phases will surely follow suit. Here, blue (BP<sup>\*</sup>) [210], twist-bend nematic (N<sub>TB</sub>) [211], TGB<sup>\*</sup> [212], or Bx (B2 [213], B4 [168], etc.) phases among others will likely see increased research activities in the coming years. Furthermore, realizing helical assemblies of nanomaterials using both thermotropic as well as lyotropic LC structures has been in increasing demand for nanomaterials exhibiting CPL properties with high and most importantly tuneable  $g_{lum}$  values. Suitably functionalized nanomaterials such as metallic (plasmonic), semiconducting, (emissive) carbon-based, polymeric and magnetic nanomaterials varying in size,

shape and aspect ratio can now be positioned with reasonably good control in the phase structures formed by LC molecules (self-assembly approach). With the precision of such processes further improving, the resulting dynamic assemblies will potentially rival and even outperform chiral nanostructures created by micro- and nanofabrication (*e.g.* lithographic, etching, deposition) techniques [214].

The all-pervasive presence of homochirality in nature still demands answers about the efficiency and pathways of chirality transfer as well as new innovative tools and methods to measure this [215]. A combination of the liquid crystalline state and materials at the nanoscale will continue to provide a rich playing field for discovery and innovation. Nevertheless, this field, while young, also needs to experience an evolution from fundamental research curiosity to devices and processes available or applied in commercial applications. Thus far, CPL materials based on the nano/LC chiral combination appear to be best positioned for this transition.

#### Acknowledgments

Some of the work by the authors highlighted in this review was supported by the U.S. National Science Foundation (NSF; DMR-1506018, CHE-1659571, ECCS-1807364, DMR-1904091) and the Ohio Third Frontier (OTF) program for Ohio Research Scholars ‘Research Cluster on Surfaces in Advanced Materials’ (T.H.). We further thank Hossien Mirzajani for providing some of the drawings.

#### Disclosure statement

No potential conflict of interest was reported by the author(s).

#### Funding

This work was supported by Division of Chemistry [Grant Number 1659571]; Division of Electrical, Communications and Cyber Systems [Grant Number 1807364]; Division of Materials Research [Grant Number 1506018,1904091].

#### ORCID

Diana P. N. Gonçalves  <http://orcid.org/0000-0003-3989-6767>

Marianne E. Prévôt  <http://orcid.org/0000-0002-1828-414X>

Şenay Üstünel  <http://orcid.org/0000-0001-7860-3870>

Timothy Ogolla  <http://orcid.org/0000-0001-9284-4187>

Ahلام Nemati  <http://orcid.org/0000-0003-0282-2027>

Sasan Shadpour  <http://orcid.org/0000-0001-9736-7295>

Torsten Hegmann  <http://orcid.org/0000-0002-6664-6598>

#### References

- [1] Ma W, Xu L, de Moura AF, et al. Chiral inorganic nanostructures. *Chem Rev.* 2012;117:8041–8093.

- [2] Brust M, Walker M, Bethell D, et al. Synthesis of thiol-derivatised gold nanoparticles in a two-phase liquid-liquid system. *J Chem Soc Chem Commun.* 1994; 801–802.
- [3] Brust M, Fink J, Bethell D, et al. Synthesis and reactions of functionalised gold nanoparticles. *J Chem Soc Chem Commun.* 1995: 1655–1656.
- [4] Schaaf TG, Knight G, Shafiqulin MN, et al. Isolation and selected properties of a 10.4 kDa gold:glutathione cluster compound. *J Phys Chem B.* 1998;102(52):10643–10646.
- [5] Schaaf TG, Whetten RL. Giant gold–glutathione cluster compounds: intense optical activity in metal-based transitions. *J Phys Chem B.* 2000;104(12):2630–2641.
- [6] Jadzinsky PD, Calero G, Ackerson CJ, et al. Structure of a thiol monolayer-protected gold nanoparticle at 1.1 angstrom resolution. *Science.* 2007;318:430–433.
- [7] Knoppe S, Bürgi T. Chirality in thiolate-protected gold clusters. *Acc Chem Res.* 2014;47:1318–1326.
- [8] Li G, Jin R. Atomically precise gold nanoclusters as new model catalysts. *Acc Chem Res.* 2013;46(8):1749–1758.
- [9] Qian H, Zhu M, Wu Z, et al. Quantum sized gold nanoclusters with atomic precision. *Acc Chem Res.* 2012;45(9):1470–1479.
- [10] Malola S, Häkkinen H. Chiral inversion of thiolate-protected gold nanoclusters via core reconstruction without breaking a Au–S bond. *J Am Chem Soc.* 2019;141(14):6006–6012.
- [11] Li Y, Higaki T, Du X, et al. Chirality and surface bonding correlation in atomically precise metal nanoclusters. *Adv Mater.* 2020;32(41):e1905488.
- [12] Yan J, Feng W, Kim JY, et al. Self-assembly of chiral nanoparticles into semiconductor helices with tunable near-infrared optical activity. *Chem Mater.* 2020;32(1): 476–488.
- [13] Đorđević L, Arcudi F, D’Urso A, et al. Design principles of chiral carbon nanodots help convey chirality from molecular to nanoscale level. *Nat Commun.* 2018;9:3442.
- [14] Fan J, Kotov NA. Chiral nanoceramics. *Adv Mater.* 2020;32:1906738.
- [15] Kane-Maguire LAP, Wallace GG. Chiral conducting polymers. *Chem Soc Rev.* 2010;39:2545–2576.
- [16] Liu M, Zhang L, Wang T. Supramolecular chirality in self-assembled systems. *Chem Rev.* 2015;115:7304–7397.
- [17] Yeom J, Santos US, Chekini M, et al. Chiro-magnetic nanoparticles and gels. *Science.* 2018;359(6373): 309–314.
- [18] Morrow SM, Bisette AJ, Fletcher SP. Transmission of chirality through space and across length scales. *Nat Nanotechnol.* 2017;12:410–419.
- [19] Zhang H, Li S, Hao C, et al. Engineering of chiral nanomaterials for biomimetic catalysis. *Chem Sci.* 2020;11:12937–12954.
- [20] Sun M, Li S, Xu C, et al. Chiral nanoprobe and their biological effects. *Chin J Chem.* 2021;39:25–31.
- [21] Tang Z. Chiral nanomaterials: preparation, properties and applications. Weinheim: Wiley-VCH; 2018.
- [22] Hegmann T, Qi H, Marx VM. Nanoparticles in liquid crystals: synthesis, self-assembly, defect formation and potential applications. *J Inorg Organomet Polym Mater.* 2007;17(3):483–508.
- [23] Stamatiou O, Mirzaei J, Feng X, et al. Nanoparticles in liquid crystals and liquid crystalline nanoparticles. *Top Curr Chem.* 2011;318:331–394.
- [24] Shivakumar U, Mirzaei J, Feng X. Nanoparticles: complex and multifaceted additives for liquid crystals. *Liq Cryst.* 2011;38(11-12):1495–1514.
- [25] Umadevi S, Ganesh V, Hegmann T, et al. Nanoparticles: additives and building blocks for liquid crystal phases. In: Goodby JW, Collings PJ, Kato T, editor. *Handbook of liquid crystals* (2nd ed.) vol. 6, ch. 2. Weinheim: Wiley-VCH; 2014. p. 27–76.
- [26] Bahr C, Kitzerow HS. Chirality in liquid crystals. New York: Springer-Verlag; 2001.
- [27] Dierking I. Chiral liquid crystals: structures, phases, effects. *Symmetry (Basel).* 2014;6:444–472.
- [28] Yang J, Zhao W, He W, et al. Liquid crystalline blue phase materials with three-dimensional nanostructures. *J Mater Chem C.* 2019;7(43):13352–13366.
- [29] Hough LE, Jung HT, Krüerke D, et al. Helical nanofilament phases. *Science.* 2009;325(5939):456–460.
- [30] Hein JE, Tse E, Blackmond DG. A route to enantiopure RNA precursors from nearly racemic starting materials. *Nat Chem.* 2011;3:704–706.
- [31] Laurent G, Lacoste D, Gaspard P. Emergence of homochirality in large molecular systems. *Proc Natl Acad Sci USA.* 2021;118(3):e2012741118.
- [32] Blackmond DG. The origin of biological homochirality. *Cold Spring Harb Perspect Biol.* 2010;2:a002147.
- [33] Sharma A, More T, Lee HC, et al. Detecting, visualizing, and measuring gold nanoparticle chirality using helical pitch measurements in nematic liquid crystal phases. *ACS Nano.* 2014;8(12):11966–11976.
- [34] Karimova N, Aikens CM. Chiral noble metal nanoparticles and nanostructures. *Part Part Syst Charact.* 2019;36:1900043.
- [35] Goldsmith MR, George C, Zuber G, et al. The chiroptical signature of achiral metal clusters induced by dissymmetric adsorbates. *Phys Chem Chem Phys.* 2006;8:63–67.
- [36] Pour SO, Rocks L, Faulds K, et al. The chiroptical signature of achiral metal clusters induced by dissymmetric adsorbates. *Nat Chem.* 2015;7:591–596.
- [37] Qi H, Hegmann T. Postsynthesis racemization and place exchange reactions. another step to unravel the origin of chirality for chiral ligand-capped gold nanoparticles. *J Am Chem Soc.* 2008;130(43):14201–14206.
- [38] Govorov AO, Gun’ko YK, Slocik JM, et al. Chiral nanoparticle assemblies: circular dichroism, plasmonic interactions, and exciton effects. *J Mater Chem.* 2011;21:16806–16818.
- [39] Dolamic I, Varnholt B, Bürgi T. Chirality transfer from gold nanocluster to adsorbate evidenced by vibrational circular dichroism. *Nat Commun.* 2015;6: 7117.
- [40] Pelayo JJ, Whetten RL, Garzón IL. Geometric quantification of chirality in ligand-protected metal clusters. *J Phys Chem C.* 2015;119(51):28666–28678.
- [41] Mori T, Sharma A, Hegmann T. Significant enhancement of the chiral correlation length in nematic liquid crystals by gold nanoparticle surfaces featuring axially chiral binaphthyl ligands. *ACS Nano.* 2016;10:1552–1564.



- [42] Noguez C, Garzoń IL. Optically active metal nanoparticles. *Chem Soc Rev*. 2009;38:757–771.
- [43] Rožič B, Fresnais J, Molinaro C, et al. Oriented gold nanorods and gold nanorod chains within smectic liquid crystal topological defects. *ACS Nano*. 2017;11(7):6728–6738.
- [44] Nemati A, Shadpour S, Querciagrossa L, et al. Chirality amplification by desymmetrization of chiral ligand-capped nanoparticles to nanorods quantified in soft condensed matter. *Nat Commun*. 2018;9:3908.
- [45] Rhee H, Choi JS, Starling DJ, et al. Amplifications in chiroptical spectroscopy, optical enantioselectivity, and weak value measurement. *Chem Sci*. 2013;4:4107–4114.
- [46] Guerrero-Martínez A, Alonso-Gómez JL, Auguie B, et al. From individual to collective chirality in metal nanoparticles. *Nano Today*. 2011;6(4):381–400.
- [47] Berardi R, Cainelli G, Galetti P, et al. Can the pi-facial selectivity of solvation be predicted by atomistic simulation? *J Am Chem Soc*. 2005;127:10699–10706.
- [48] Pietropaolo A, Muccioli L, Berardi R, et al. A chirality index for investigating protein secondary structures and their time evolution. *Proteins Struct Funct Genet*. 2008;70:667–677.
- [49] Almeida A, Querciagrossa L, Silva P, et al. Reversible water driven chirality inversion in cellulose-based helices from erodium awns. *Soft Matter*. 2019;15:2838–2847.
- [50] Nemati A, Shadpour S, Querciagrossa L, et al. Highly sensitive, tunable chirality amplification through space visualized for gold nanorods capped with axially chiral binaphthyl derivatives. *ACS Nano*. 2019;13:10312–10326.
- [51] Yu H, Welch C, Qu W, et al. Chirality enhancement in macro-chiral liquid crystal nanoparticles. *Mater Horizons*. 2020;7:3021–3027.
- [52] Cseh L, Mang X, Zeng X, et al. Helically twisted chiral arrays of gold nanoparticles coated with a cholesterol mesogen. *J Am Chem Soc*. 2015;137:12736–12739.
- [53] Bhat SA, Shankar Rao DS, Krishna Prasad S, et al. Chiral plasmonic liquid crystal gold nanoparticles: self-assembly into a circular dichroism responsive helical lamellar superstructure. *Nanoscale Adv*. 2021;3:2269–2279.
- [54] Bhardwaj A, Sridurai V, Bhat SA, et al. Photo-tunable epsilon-near-zero behavior in a self-assembled liquid crystal – nanoparticle hybrid material. *Nanoscale Adv*. 2021; doi:10.1039/d0na01039a.
- [55] Perera K, Nemati A, Mann EK, et al. Converging microlens array using nematic liquid crystals doped with chiral nanoparticles. *ACS Appl Mater Interfaces*. 2021;13(3):4574–4582.
- [56] Pinkert A, Marsh KN, Pang S, et al. Ionic liquids and their interaction with cellulose. *Chem Rev*. 2009;109(12):6712–6728.
- [57] Moon RJ, Martini A, Nairn J, et al. Cellulose nanomaterials review: structure, properties and nanocomposites. *Chem Soc Re*. 2011;40(7):3941–3994.
- [58] Rånby BG. Aqueous colloidal solutions of cellulose micelles. *Acta Chem Scand*. 1949;3:649–450.
- [59] Peng BL, Dhar N, Liu HL, et al. Chemistry and applications of nanocrystalline cellulose and its derivatives: A nanotechnology perspective. *Can J Chem Eng*. 2011;89(5):1191–1206.
- [60] Tran A, Boott CE, MacLachlan MJ. Understanding the self-assembly of cellulose nanocrystals-toward chiral photonic materials. *Adv Mater*. 2020;32(41):1905876.
- [61] Grishkewich N, Mohammed N, Tang J, et al. Recent advances in the application of cellulose nanocrystals. *Curr Opin Coll Interf Sci*. 2017;29:32–45.
- [62] Klemm D, Kramer F, Moritz S, et al. Nanocelluloses: a new family of nature-based materials. *Angew Chem Int Ed Engl*. 2011;50(24):5438–5466.
- [63] Belbekhouche S, Bras J, Siqueira G, et al. Water sorption behavior and gas barrier properties of cellulose whiskers and microfibrils films. *Carbohydrate Polym*. 2011;83(4):1740–1748.
- [64] Mueller S, Sapkota J, Nicharat A, et al. Influence of the nanofiber dimensions on the properties of nanocellulose/poly(vinyl alcohol) aerogels. *J Appl Polym Sci*. 2015;132(13):41740.
- [65] Ustunel S, Prévôt ME, Rohaley GAR, et al. Mechanically tunable elastomer and cellulose nanocrystal composites as scaffolds for in vitro cell studies. *Mater Adv*. 2021;2:464–476.
- [66] Jackson JK, Letchford K, Wasserman BZ, et al. The use of nanocrystalline cellulose for the binding and controlled release of drugs. *Int J Nanomed*. 2011;6:321–330.
- [67] Revol JE, Bradford H, Giasson J, et al. Helicoidal self-ordering of cellulose microfibrils in aqueous suspension. *Int J Biol Macromol*. 1992;14(3):170–172.
- [68] Marchessault R, Morehead F, Walter N. Liquid crystal systems from fibrillar polysaccharides. *Nature*. 1959;184:632–633.
- [69] Revol J, Godbout L, Gray D. Solid self-assembled films of cellulose with chiral nematic order and optically variable properties. *J Pulp Pap Sci*. 1998;24(5):146–149.
- [70] Dionne GF, Allen GA, Haddad PR, et al. Circular polarization and nonreciprocal propagation in magnetic media. *Lincoln Lab J*. 2005;15(2):323–340.
- [71] de Vries H. Rotatory power and other optical properties of certain liquid crystals. *Acta Crystallogr*. 1951;4:219–226.
- [72] Lagerwall JPF, Schütz C, Salajkova M, et al. Cellulose nanocrystal-based materials: from liquid crystal self-assembly and glass formation to multifunctional thin films. *NPG Asia Mater*. 2014;6(1):e80–e80.
- [73] Edgar CD, Gray DG. Induced circular dichroism of chiral nematic cellulose films. *Cellulose*. 2001;8:5–12.
- [74] Zhang YP, Chodavarapu V, Kirk A, et al. Nanocrystalline cellulose for covert optical encryption. *J Nanophoton*. 2012;6(1):063516.
- [75] Shopsowitz KE, Qi H, Hamad WY, et al. Free-standing mesoporous silica films with tunable chiral nematic structures. *Nature*. 2010;468(7322):422–425.
- [76] Querejeta-Fernandez A, Chauve G, Methot M, et al. Chiral plasmonic films formed by gold nanorods and cellulose nanocrystals. *J Am Chem Soc*. 2014;136(12):4788–4793.

- [77] Lukach A, Therien-Aubin H, Querejeta-Fernandez A, et al. Coassembly of gold nanoparticles and cellulose nanocrystals in composite films. *Langmuir*. 2015;31(18):5033–5041.
- [78] Zheng H, Li W, Li W, et al. Uncovering the circular polarization potential of chiral photonic cellulose films for photonic applications. *Adv Mater*. 2018;30(13):1705948.
- [79] Hiratani T, Hamad WY, MacLachlan MJ. Transparent depolarizing organic and inorganic films for optics and sensors. *Adv Mater*. 2017;29(13):1606083.
- [80] Li W, Xu M, Ma C, et al. Tunable upconverted circularly polarized luminescence in cellulose nanocrystal based chiral photonic films. *ACS Appl Mater Interfaces*. 2019;11(26):23512–23519.
- [81] Xu M, Li W, Ma C, et al. Multifunctional chiral nematic cellulose nanocrystals/glycerol structural colored nanocomposites for intelligent responsive films, photonic inks and iridescent coatings. *J Mater Chem C*. 2018;6(20):5391–5400.
- [82] Xiong R, Yu S, Smith MJ, et al. Self-assembly of emissive nanocellulose/quantum dot nanostructures for chiral fluorescent materials. *ACS Nano*. 2019;13(8):9074–9081.
- [83] Xu M, Wu X, Yang Y, et al. Designing hybrid chiral photonic films with circularly polarized room-temperature phosphorescence. *ACS Nano*. 2020;14(9):11130–11139.
- [84] Habibi Y, Lucia LA, Rojas OJ. Cellulose nanocrystals: chemistry, self-assembly, and applications. *Chem Rev*. 2010;110(6):3479–3500.
- [85] Islam MS, Chen L, Sisler J, et al. Cellulose nanocrystal (CNC)–inorganic hybrid systems: synthesis, properties and applications. *J Mater Chem B*. 2018;6(6):864–883.
- [86] Xia Y, Zhou Y, Tang Z. Chiral inorganic nanoparticles: origin, optical properties and bioapplications. *Nanoscale*. 2011;3(4):1374–1382.
- [87] Mahpeykar SM, Zhao Y, Li X, et al. Cellulose nanocrystal:polymer hybrid optical diffusers for index-matching-free light management in optoelectronic devices. *Adv Opt Mater*. 2017;5(21):1700430.
- [88] Gubler U, Bosshard C. Optical materials: A new twist for nonlinear optics. *Nat Mater*. 2002;1(4):209–210.
- [89] Tang Y, Cohen AE. Enhanced enantioselectivity in excitation of chiral molecules by superchiral light. *Science*. 2011;332(6027):333–336.
- [90] Yu LJ, Saupe A. Liquid crystalline phases of the sodium decylsulfate/decanol/water system. nematic-nematic and cholesteric-cholesteric phase transitions. *J Am Chem Soc*. 1980;102:4879–4883.
- [91] Lawson KD, Flautt TJ. Magnetically oriented lyotropic liquid crystalline phases. *J Am Chem Soc*. 1967;89:5489–5491.
- [92] Tiddy GJT. Surfactant-water liquid crystal phases. *Phys Rep*. 1980;57:1–46.
- [93] Collings PJ, Dickinson AJ, Smith EC. Molecular aggregation and chromonic liquid crystals. *Liq Cryst*. 2010;37:701–710.
- [94] Lydon J. Chromonic liquid crystalline phases. *Liq Cryst*. 2011;38:1663–1681.
- [95] Tam-Chang SW, Huang L. Chromonic liquid crystals: properties and applications as functional materials. *Chem Commun*. 2008;0:1957–1967.
- [96] Livolant F, Levelut AM, Doucet J, et al. The highly concentrated liquid-crystalline phase of DNA is columnar hexagonal. *Nature*. 1989;339:724–726.
- [97] Zanchetta G, Bellini T, Nakata M, et al. Physical polymerization and liquid crystallization of RNA oligomers. *J Am Chem Soc*. 2008;130:12864–12865.
- [98] Bernal JD, Fankuchen I. X-ray and crystallographic studies of plant virus preparations. *J Gen Physiol*. 1941;25:111–146.
- [99] Gregory J, Holmes KC. Methods of preparing orientated tobacco mosaic virus sols for X-ray diffraction. *J Mol Biol*. 1965;13:796–815.
- [100] Sonin AS. Inorganic lyotropic liquid crystals. *J Mater Chem*. 1998;8:2557–2574.
- [101] Dietrich CF, Collings PJ, Sottmann T, et al. Extremely small twist elastic constants in lyotropic nematic liquid crystals. *Proc Natl Acad Sci USA*. 2020;117:27238–27244.
- [102] Jeong J, Davidson ZS, Collings PJ, et al. Chiral symmetry breaking and surface faceting in chromonic liquid crystal droplets with giant elastic anisotropy. *Proc Natl Acad Sci USA*. 2014;111:1742–1747.
- [103] Jeong J, Kang L, Davidson ZS, et al. Chiral structures from achiral liquid crystals in cylindrical capillaries. *Proc Natl Acad Sci USA*. 2015;112:E1837–E1844.
- [104] Zhou S, Neupane K, Nastishin YA, et al. Elasticity, viscosity, and orientational fluctuations of a lyotropic chromonic nematic liquid crystal disodium cromoglycate. *Soft Matter*. 2014;10:6571–6581.
- [105] Tortora L, Lavrentovich OD. Chiral symmetry breaking by spatial confinement in tactoidal droplets of lyotropic chromonic liquid crystals. *Proc Natl Acad Sci USA*. 2011;108:5163–5168.
- [106] Dietrich CF, Rudquist P, Collings PJ, et al. Interplay between confinement, twist elasticity, and intrinsic chirality in micellar lyotropic nematic liquid crystals. *Langmuir*. 2021;37:2749–2758.
- [107] Park G, Čopar S, Suh A, et al. Periodic arrays of chiral domains generated from the self-assembly of micropatterned achiral lyotropic chromonic liquid crystal. *ACS Cent Sci*. 2020;6:1964–1970.
- [108] Peng C, Lavrentovich OD. Chirality amplification and detection by tactoids of lyotropic chromonic liquid crystals. *Soft Matter*. 2015;11:7257–7263.
- [109] Shadpour S, Vanegas JP, Nemati A, et al. Amplification of chirality by adenosine monophosphate-capped luminescent gold nanoclusters in nematic lyotropic chromonic liquid crystal tactoids. *ACS Omega*. 2019;4:1662–1668.
- [110] Zimmermann N, Jünnemann-Held G, Collings PJ, et al. Self-organized assemblies of colloidal particles obtained from an aligned chromonic liquid crystal dispersion. *Soft Matter*. 2015;11:1547–1553.
- [111] Nych A, Ognysta U, Muševič I, et al. Chiral bipolar colloids from nonchiral chromonic liquid crystals. *Phys Rev E*. 2014;89:062502.
- [112] Bergquist L, Hegmann T. Chiral amplification by L-cysteine-capped gold nanoparticles in lyotropic chromonic liquid crystals. *Chem Nano Mat*. 2017;3:863–868.
- [113] West JL, Glushchenko A, Liao G, et al. Drag on particles in a nematic suspension by a moving nematic-isotropic interface. *Phys Rev E*. 2002;66:012702.

- [114] Yashima E, Maeda K, Iida H, et al. Helical polymers: synthesis, structures, and functions. *Chem Rev.* 2009;109(11):6102–6211.
- [115] Kumar J, Thomas KG, Liz-Marzán LM. Nanoscale chirality in metal and semiconductor nanoparticles. *Chem Commun.* 2016;52(85):12555–12569.
- [116] Kumar J, Eraña H, López-Martínez E, et al. Detection of amyloid fibrils in Parkinson's disease using plasmonic chirality. *Proc. Natl Acad Sci.* 2018;115(13):3225–3230.
- [117] Kim Y, Yeom B, Arteaga O, et al. Reconfigurable chiroptical nanocomposites with chirality transfer from the macro- to the nanoscale. *Nat Mater.* 2016;15(4):461–468.
- [118] Lan X, Wang Q. Self-assembly of chiral plasmonic nanostructures. *Adv Mater.* 2016;28(47):10499–10507.
- [119] Zhang DW, Li M, Chen CF. Recent advances in circularly polarized electroluminescence based on organic light-emitting diodes. *Chem Soc Rev.* 2020;49(5):1331–1343.
- [120] Farshchi R, Ramsteiner M, Herfort J, et al. Optical communication of spin information between light emitting diodes. *Appl Phys Lett.* 2011;98(16):162508.
- [121] Sherson JF, Krauter H, Olsson RK, et al. Quantum teleportation between light and matter. *Nature.* 2006;443(7111):557–560.
- [122] Schadt M. Liquid crystals materials and liquid crystal displays. *Ann Rev Mater Sci.* 1997;27:305–379.
- [123] Kim DY. Potential application of spintronic light-emitting diode to binocular vision for three-dimensional display technology. *J Korean Phys Soc.* 2006;49:505–508.
- [124] Brandt JR, Salerno F, Fuchter MJ. The added value of small-molecule chirality in technological applications. *Nature Rev Chem.* 2017;1:0045.
- [125] Zhao Y, Xu L, Ma W, et al. Shell-engineered chiroplasmonic assemblies of nanoparticles for zeptomolar DNA detection. *Nano Lett.* 2014;14(7):3908–3913.
- [126] Okutani K, Nozaki K, Iwamura M. Specific chiral sensing of amino acids using induced circularly polarized luminescence of bis(diimine)dicarboxylic acid europium(III) complexes. *Inorg Chem.* 2014;53(11):5527–5537.
- [127] Shuvaev S, Sutturina EA, Mason K, et al. Chiral probes for  $\alpha$ 1-AGP reporting by species-specific induced circularly polarised luminescence. *Chem Sci.* 2018;9(11):2996–3003.
- [128] Heffern MC, Matosziuk LM, Meade TJ. Lanthanide probes for bioresponsive imaging. *Chem Rev.* 2014;114(8):4496–4539.
- [129] Chen C, Gao L, Gao W, et al. Circularly polarized light detection using chiral hybrid perovskite. *Nat Commun.* 2019;10:1927.
- [130] Zhao T, Han J, Duan P, et al. New perspectives to trigger and modulate circularly polarized luminescence of complex and aggregated systems: energy transfer, photon upconversion, charge transfer, and organic radical. *Acc Chem Res.* 2020;53(7):1279–1292.
- [131] Zinna F, Di Bari L. Lanthanide circularly polarized luminescence: bases and applications. *Chirality.* 2015;27(1):1–13.
- [132] Lunkley JL, Shirovani D, Yamanari K, et al. Extraordinary circularly polarized luminescence activity exhibited by cesium tetrakis (3-heptafluoro-butylryl-(+)- camphorato) Eu(III) complexes in EtOH and CHCl<sub>3</sub> solutions. *J Am Chem Soc.* 2008;130(42):13814–13815.
- [133] Sánchez-Carnerero EM, Agarrabeitia AR, Moreno F, et al. Circularly polarized luminescence from simple organic molecules. *Chem Eur J.* 2015;21(39):13488–13500.
- [134] Green MM, Park J-W, Sato T, et al. The macromolecular route to chiral amplification. *Angew Chem Int Ed.* 1999;38(21):3138–3154.
- [135] Yashima E, Ousaka N, Taura D, et al. Supramolecular helical systems: helical assemblies of small molecules, foldamers, and polymers with chiral amplification and their functions. *Chem Rev.* 2016;116(22):13752–13990.
- [136] Watanabe K, Akagi K. Helically assembled  $\pi$ -conjugated polymers with circularly polarized luminescence. *Sci Technol Adv Mater.* 2014;15(4):044203.
- [137] Kumar J, Nakashima T, Tsumatori H, et al. Circularly polarized luminescence in chiral aggregates: dependence of morphology on luminescence dissymmetry. *J Phys Chem Lett.* 2014;5(2):316–321.
- [138] Ma K, Chen W, Jiao T, et al. Boosting the circularly polarized luminescence of small organic molecules via multi-dimensional morphology control. *Chem Sci.* 2019;10(28):6821–6827.
- [139] Mei J, Leung NLC, Kwok RTK, et al. Aggregation-induced emission: together we shine, united we soar!. *Chem Rev.* 2015;115(21):11718–11940.
- [140] Leung NLC, Xie N, Yuan W, et al. Restriction of intramolecular motions: the general mechanism behind aggregation-induced emission. *Chem Eur J.* 2014;20(47):15349–15353.
- [141] Liu J, Su H, Meng L, et al. What makes efficient circularly polarized luminescence in the condensed phase: aggregation-induced circular dichroism and light emission. *Chem Sci.* 2012;3(9):2737.
- [142] Lu N, Gao X, Pan M, et al. Aggregation-induced emission-active chiral helical polymers show strong circularly polarized luminescence in thin films. *Macromolecules.* 2020;53(18):8041–8049.
- [143] Harada T, Kajiyama N, Ishizaka K, et al. Plasmon resonance-enhanced circularly polarized luminescence of self-assembled meso-tetrakis(4-sulfonatophenyl)porphyrin-surfactant complexes in interaction with Ag nanoparticles. *Chem Commun.* 2014;50(76):11169–11172.
- [144] Shi N, Wang R, Wang X, et al. Surface plasmon resonance-assisted circularly polarized luminescent hybrid assemblies of Eu-containing polyoxometalates. *Chem Commun.* 2019;55(8):1136–1139.
- [145] Yang D, Duan P, Zhang L, et al. Chirality and energy transfer amplified circularly polarized luminescence in composite nanohelix. *Nat Commun.* 2017;8:15727.
- [146] Han J, Duan P, Li X, et al. Amplification of circularly polarized luminescence through triplet-triplet annihilation-based photon upconversion. *J Am Chem Soc.* 2017;139(29):9783–9786.
- [147] San Jose BA, Yan J, Akagi K. Dynamic switching of the circularly polarized luminescence of disubstituted polyacetylene by selective transmission through a thermotropic chiral nematic liquid crystal. *Angew Chem Int Ed.* 2014;53(40):10641–10644.
- [148] Wood S, Prévôt ME, Amela-Cortes M, et al. Polarized phosphorescence of isotropic and metal-based clustomesogens dispersed into chiral nematic liquid



- crystalline films. *Adv Opt Mater.* **2015**;3(10):1368–1372.
- [149] Yang X, Zhou M, Wang Y, et al. Electric-field-regulated energy transfer in chiral liquid crystals for enhancing upconverted circularly polarized luminescence through steering the photonic bandgap. *Adv Mater.* **2020**;32(24):2000820.
- [150] Juan A, Lin S, He Y, et al. Near-infrared light-induced photoisomerization and photodissociation of a chiral fluorescent photoswitch in cholesteric liquid crystals assisted by upconversion nanoparticles. *Soft Matter.* **2021**;17:1404–1408.
- [151] Di Nuzzo D, Kulkarni C, Zhao B, et al. High circular polarization of electroluminescence achieved via self-assembly of a light-emitting chiral conjugated polymer into multidomain cholesteric films. *ACS Nano.* **2017**;11(12):12713–12722.
- [152] Prévôt ME, Vanegas JP, Hegmann E, et al. Emissive nanomaterials and liquid crystals. In: Sattler KD, editor. *21st century nanoscience – A handbook: exotic nanostructures and quantum systems (1st ed.)*. Boca Raton: CRC Press; **2020**. p. 1–16.
- [153] Chen D, Maclennan JE, Shao R, et al. Chirality-preserving growth of helical filaments in the B4 phase of bent-core liquid crystals. *J Am Chem Soc.* **2011**;133(32):12656–12663.
- [154] Grason GM. Perspective: geometrically frustrated assemblies. *J Chem Phys.* **2016**;145(11):110901.
- [155] Li L, Salamończyk M, Shadpour S, et al. An unusual type of polymorphism in a liquid crystal. *Nat Commun.* **2018**;9(1):1–8.
- [156] Shadpour S, Nemati A, Boyd NJ, et al. Heliconical-layered nanocylinders (HLNCs)–hierarchical self-assembly in a unique B4 phase liquid crystal morphology. *Mater Horizons.* **2019**;6(5):959–968.
- [157] Tsai E, Richardson JM, Körblová E, et al. A modulated helical nanofilament phase. *Angew Chem Int Ed Engl.* **2013**;125(20):5362–5365.
- [158] Li L, Salamończyk M, Jáklí A, et al. A dual modulated homochiral helical nanofilament phase with local columnar ordering formed by bent core liquid crystals: effects of molecular chirality. *Small.* **2016**;12(29):3944–3955.
- [159] Shadpour S, Nemati A, Salamończyk M, et al. Missing Link between helical nano- and microfilaments in B4 phase bent-core liquid crystals, and deciphering which chiral center controls the filament handedness. *Small.* **2020**;16(4):1905591.
- [160] Liu J, Shadpour S, Prévôt ME, et al. Molecular conformation of bent-core molecules affected by chiral side chains dictates polymorphism and chirality in organic nano- and microfilaments. *ACS Nano.* **2021**; doi:10.1021/acsnano.1c00527.
- [161] Walba DM, Eshdat L, Körblová E, et al. On the nature of the B4 banana phase: crystal or not a crystal? *Cryst Growth Des.* **2005**;5(6):2091–2099.
- [162] Araoka F, Sugiyama G, Ishikawa K, et al. Highly ordered helical nanofilament assembly aligned by a nematic director field. *Adv Funct Mater.* **2013**;23(21):2701–2707.
- [163] Park W, Yoon DK. Orientation control of helical nanofilament phase and its chiroptical applications. *Crystals (Basel).* **2020**;10(8):675.
- [164] Park W, Ha T, Kim TT, et al. Directed self-assembly of a helical nanofilament liquid crystal phase for use as structural color reflectors. *NPG Asia Mater.* **2019**;11(1):1–8.
- [165] Yoon DK, Yi Y, Shen Y, et al. Orientation of a helical nanofilament (B4) liquid-crystal phase: topographic control of confinement, shear flow, and temperature gradients. *Adv Mater.* **2011**;23(17):1962–1967.
- [166] Kim H, Lee S, Shin TJ, et al. Multistep hierarchical self-assembly of chiral nanopore arrays. *Proc. Natl Acad Sci USA.* **2014**;111(40):14342–14347.
- [167] Park W, Wolska JM, Pocięcha D, et al. Direct visualization of optical activity in chiral substances using a helical nanofilament (B4) liquid crystal phase. *Adv Opt Mater.* **2019**;7(23):1901399.
- [168] Bagiński M, Tupikowska M, González-Rubio G, et al. Shaping liquid crystals with gold nanoparticles: helical assemblies with tunable and hierarchical structures via thin-film cooperative interactions. *Adv Mater.* **2020**;32(1):1904581.
- [169] Zhu C, Chen D, Shen Y, et al. Nanophase segregation in binary mixtures of a bent-core and a rodlike liquid-crystal molecule. *Phys Rev E.* **2010**;81(1):011704.
- [170] Chen D, Zhu C, Wang H. Nanoconfinement of guest materials by helical nanofilament networks of bent-core mesogens. *Soft Matter.* **2013**;9:462–471.
- [171] Chen D, Tuchband MR, Horanyi B, et al. Diastereomeric liquid crystal domains at the mesoscale. *Nat Commun.* **2015**;6:7763.
- [172] Gorecka E, Vaupotič N, Zep A, et al. From sponges to nanotubes: A change of nanocrystal morphology for acute-angle bent-core molecules. *Angew Chem.* **2016**;128(40):12426–12430.
- [173] Liu J, Shadpour S, Nemati A, et al. Binary mixtures of bent-core molecules forming distinct types of B4 phase nano- and microfilament morphologies. *Liq Cryst.* **2020**; doi:10.1080/02678292.2020.1847333.
- [174] Umadevi S, Feng X, Hegmann T. Large area self-assembly of nematic liquid-crystal-functionalized gold nanorods. *Adv Funct Mater.* **2013**;23:1393–1403.
- [175] Feng X, Sosa-Vargas L, Umadevi S, et al. Discotic liquid crystal-functionalized gold nanorods: 2- and 3D self-assembly and macroscopic alignment as well as increased charge carrier mobility in hexagonal columnar liquid crystal hosts affected by molecular packing and  $\pi$ - $\pi$  interactions. *Adv Funct Mater.* **2015**;25:1180–1192.
- [176] Szustakiewicz P, Kowalska N, Grzelak D, et al. Supramolecular chirality synchronization in thin films of plasmonic nanocomposites. *ACS Nano.* **2020**;14(10):12918–12928.
- [177] Lu J, Xue Y, Bernardino K, et al. Enhanced optical asymmetry in supramolecular chiroplasmonic assemblies with long-range order. *Science.* **2021**;371(6536):1368–1374.
- [178] Lee J-J, Kim B-C, Choi H-J, et al. Inverse helical nanofilament networks serving as a chiral nanotemplate. *ACS Nano.* **2020**;14(5):5243–5250.
- [179] Jiang W, Qu Z-B, Kumar P, et al. Emergence of complexity in hierarchically organized chiral particles. *Science.* **2020**;368(6491):642–648.
- [180] Xia Y, Nguyen TD, Yang M, et al. Self-assembly of self-limiting monodisperse supraparticles from polydisperse nanoparticles. *Nat Nanotechnol.* **2011**;6(9):580–587.

- [181] Oda R, Huc I, Schmutz M, et al. Tuning bilayer twist using chiral counterions. *Nature*. 1999;399(6736):566–569.
- [182] Li Y, Li GT, Wang XY, et al. Unique twisted ribbons generated by self-assembly of oligo(*p*-phenylene ethylene) bearing dimeric bile acid pendant groups. *Chem Eur J*. 2009;15(26):6399–6407.
- [183] Wagalgave SM, Padghan SD, Burud MD, et al. Supramolecular super-helix formation *via* self-assembly of naphthalene diimide functionalised with bile acid derivatives. *Sci Rep*. 2019;9:12825.
- [184] Budin I, Szostak JW. Expanding roles for diverse physical phenomena during the origin of life. *Annu Rev Biophys*. 2010;39:245–263.
- [185] Fraccia TP, Smith GP, Zanchetta G, et al. Abiotic ligation of DNA oligomers templated by their liquid crystal ordering. *Nat Commun*. 2015;6:1–8.
- [186] Zanchetta G, Giavazzi F, Nakata M, et al. Right-handed double-helix ultrashort DNA yields chiral nematic phases with both right- and left-handed director twist. *Proc Natl Acad Sci USA*. 2010;107:17497–17502.
- [187] Onsager L. The effects of shape on the interaction of colloidal particles. *Ann N Y Acad Sci*. 1949;51:627–659.
- [188] Fraccia TP, Smith GP, Clark NA, et al. Liquid crystal ordering of four-base-long DNA oligomers with both G-C and A-T pairing. *Crystals (Basel)*. 2018;8(1):5.
- [189] Nakata M, Zanchetta G, Chapman BD, et al. End-to-end stacking and liquid crystal condensation of 6 to 20 base pair DNA duplexes. *Science*. 2007;318:1276–1279.
- [190] Todisco M, Smith GP, Fraccia TP. Liquid crystal ordering of DNA Dickerson dodecamer duplexes with different 5'-phosphate terminations. *Mol Cryst Liq Cryst*. 2019;683:69–80.
- [191] Fraccia TP, Jia TZ. Liquid crystal coacervates composed of short double-stranded DNA and cationic peptides. *ACS Nano*. 2020;14:15071–15082.
- [192] Dietz H, Douglas SM, Shih WM. Folding DNA into twisted and curved nanoscale shapes. *Science*. 2009;325:725–730.
- [193] Douglas SM, Dietz H, Liedl T, et al. Self-assembly of DNA into nanoscale three-dimensional shapes. *Nature*. 2009;459:414–418.
- [194] Bai XC, Martin TG, Scheres SH, et al. Dietz, cryo-EM structure of a 3D DNA-origami object. *Proc Natl Acad Sci USA*. 2012;109:20012–20017.
- [195] Siavashpouri M, Wachauf C, Zakhary M, et al. Molecular engineering of chiral colloidal liquid crystals using DNA origami. *Nat Mater*. 2017;16:849–856.
- [196] Tortora MM, Mishra G, Prešern D, et al. Chiral shape fluctuations and the origin of chirality in cholesteric phases of DNA origamis. *Sci Adv*. 2020;6:eaaw8331.
- [197] Wang ZG, Song C, Ding B. Functional DNA nanostructures for photonic and biomedical applications. *Small*. 2013;9(13):2210–2222.
- [198] Kühler P, Roller EM, Schreiber R, et al. Plasmonic DNA-origami nanoantennas for surface-enhanced Raman spectroscopy. *Nano Lett*. 2014;14(5):2914–2919.
- [199] Schreiber R, Luong N, Fan Z, et al. Chiral plasmonic DNA nanostructures with switchable circular dichroism. *Nat Commun*. 2013;4:2948.
- [200] Shen X, Song C, Wang J, et al. Rolling up gold nanoparticle-dressed DNA origami into three-dimensional plasmonic chiral nanostructures. *J Am Chem Soc*. 2012;134:146–149.
- [201] Kuzyk A, Schreiber R, Zhang H, et al. Reconfigurable 3D plasmonic metamolecules. *Nat Mater*. 2014;13:862–866.
- [202] Shen B, Kostianen MA, Linko V. DNA origami nanophotonics and plasmonics at interfaces. *Langmuir*. 2018;34(49):14911–14920.
- [203] Ceconello A, Besteiro LV, Govorov AO, et al. Chiro-plasmonic DNA-based nanostructures. *Nat Rev Mater*. 2017;2:17039.
- [204] Brach K, Matczyszyn K, Olesiak-Banska J, et al. Stabilization of DNA liquid crystals on doping with gold nanorods. *Phys Chem Chem Phys*. 2016;18:7278–7283.
- [205] Atorf B, Funck T, Hegmann T, et al. Liquid crystals and precious metal: from nanoparticle dispersions to functional plasmonic nanostructures. *Liq Cryst*. 2017;44(12-13):1929–1947.
- [206] Prévôt ME, Nemati A, Cull TR, et al. A zero-power optical, ppt- to ppm-level toxic gas and vapor sensor with image, text, and analytical capabilities. *Adv Mater Technol*. 2020;5(5):2000058.
- [207] Liu L, Wang L, Qing Y, et al. Chiral nematic assemblies of silver nanoparticles in cellulose nanocrystal membrane with tunable optical properties. *J Mater Sci*. 2019;54:6699–6708.
- [208] Guo JK, Vij JK, Song JK. Tunable transfer of molecules between liquid crystal microdroplets and control of photonic crystallinity in isolated microdroplets. *Adv Opt Mater*. 2017;5:1700119.
- [209] Chiccoli C, Pasini P, Skačej G, et al. Chirality transfer from helical nanostructures to nematics: a monte carlo study. *Mol Cryst Liq Cryst*. 2013;576(1):151–156.
- [210] Gharbi MA, Manet S, Lhermitte J, et al. Reversible nanoparticle cubic lattices in blue phase liquid crystals. *ACS Nano*. 2016;10(3):3410–3415.
- [211] Paterson DA, Gao M, Kim YK, et al. Understanding the twist-bend nematic phase: the characterisation of 1-(4-cyanobiphenyl-4'-yloxy)-6-(4-cyanobiphenyl-4'-yl)hexane (CB6OCB) and comparison with CB7CB. *Soft Matter*. 2016;12:6827–6840.
- [212] Trček M, Cordoyiannis G, Tzitzios V, et al. Nanoparticle-induced twist-grain boundary phase. *Phys Rev E*. 2014;90:032501.
- [213] Marx VM, Girgis H, Heiney PA, et al. Bent-core liquid crystal (LC) decorated gold nanoclusters: synthesis, self-assembly, and effects in mixtures with bent-core LC hosts. *J Mater Chem*. 2008;18:2983–2994.
- [214] Hentschel M, Schäferling M, Duan X, et al. Chiral plasmonics. *Sci Adv*. 2017;3(5):e1602735.
- [215] Blackmond DG. The origin of biological homochirality. *CSH Perspect Biol*. 2019;11:a032540.